CWP-161
December 1994

Elimination of Numerical Dispersion in Finite-Difference Modeling and Migration by Flux-Corrected Transport

Tong Fei

— Doctoral Thesis —
Mathematical and Computer Sciences

Center for Wave Phenomena
Colorado School of Mines
Golden, Colorado 80401
303/273-3557

ABSTRACT

Finite-difference acoustic- and elastic-wave modeling and reverse-time depth migration based on the full wave equation are general approaches that can take into account arbitary variations in velocity, density and elastic coefficients, and can handle turning waves as well. However, conventional finite-difference methods for solving the acoustic- and elastic-wave equations suffer from numerical dispersion when too few samples per wavelength are used.

To reduce the numerical dispersion in finite-difference wavefield continuation, I have developed two "flux-corrected transport" (FCT) algorithms (which apply diffusion and anti-diffusion corrections to the solutions obtained by conventional methods), one based on the original second-order wave equation and the other based on a system of first-order wave equations derived from the second-order one. The key underlying assumption of the FCT method is that all local extrema are caused by numerical dispersion. Using this assumption, the FCT method first applies the diffusion correction everywhere, and then applies the anti-diffusion correction selectively, based on locations where the algorithm judges numerical dispersion to be present. In an alternative approach based on the same assumption, I have optimized the FCT approach by using only localized diffusion, with no anti-diffusion correction, at a 40 percent saving in computational cost (of the correction step) compared with that of the full FCT diffusion and anti-diffusion correction. I find that incorporating the FCT technique in conventional finite-difference modeling or reverse-time migration ensures finite-difference solutions with no numerical dispersion, even for impulsive sources.

The FCT correction, which can be applied to finite differences of any order in space and time, is an efficient alternative to use of finite-difference approximations of increasing order. For 2-D problems, the computational speed of the full FCT-corrected fourth-order finite-differencing for the second-order acoustic wave equation is about 7.7, 1.5 and 1.3 times that of the second-order, fourth-order and tenth-order conventional finite-difference methods, respectively; for 3-D problems, the increase in the speed of FCT-corrected computations is even greater. Moreover, the FCT approach applied to the fourth-order method for 3-D problems requires only about 3.8, 30 and 73 percent of the memory used by the second-order, fourth-order and tenth-order finite-difference methods, respectively. For the optimized FCT approach applied to the fourth-order method, the increase in computational speed is even greater; however, the memory usage is the same as that for the full FCT approach.

I have tested the FCT algorithms on modeling and migration for both acoustic media and elastic transversely isotropic media with vertical axis of symmetry. Moreover, I have applied the FCT correction to modeling for transversely isotropic media with tilted symmetry axis. Demonstrations of modeling and migration show benefits as well as the inability to fully recover the resolution lost when the spatial sampling becomes too coarse.

TABLE OF CONTENTS

ACKNOWLEDGMENTS

I would like to express my deepest appreciation to Prof. Ken Larner, my advisor, for his advice, encouragement and support. I specially want to thank Prof. Norman Bleistein for his help on the asymptotic analysis of the finite-difference scheme. I thank the members of the advisory committee, Prof. Jack Cohen, Joan Gosink, Steve Pruess and John Scales for their guidance and encouragement. I would also like to thank Dr. Dave Hale for helpful discussions and comments at the beginning of this research.

I gratefully acknowledge the support by the members of the Consortium Project on Seismic Inversion Methods for Complex Structures at the Center for Wave Phenomena, Colorado School of Mines. I would also like to acknowledge Los Alamos National Laboratory for providing computer (**CM5**) resources.

I deeply thank my parents, Prof. K. Fei and Mrs. C. Chen, for their encouragement and support during my graduate studies. A special thanks is expressed to my wife, Yadi Wang, for her support and help during this investigation.

Chapter 1

INTRODUCTION

Finite-difference methods, following the approaches of Claerbout (1985), have been widely implemented for wave extrapolation in modeling and migration. Those approaches employ a one-way wave equation that allows energy to propagate either downward or upward, but not both. Although successful in many situations, such methods are limited by assumptions made in deriving the one-way wave equation. Moreover, finite-difference schemes based on the one-way wave equation contain a limit on the maximum dip angle of the reflector. To overcome this limitation, Whitmore (1983) developed an iterative depth migration by backward time propagation based on the full acoustic wave equation. Loewenthal and Mufti (1983), and Kosloff and Baysal (1983) developed a two-dimensional migration scheme in the frequency and space domain based on a direct integration in depth of the acoustic wave equation, and McMechan (1985) used finite-difference modeling to study finite-offset and multiple-offset vertical seismic profile (VSP) data in laterally varying two-dimensional (2-D) media.

In seismic applications, the assumption that the medium is acoustic is not always applicable. Modeling of amplitude-versus-offset (AVO) behavior requires treatment of wave propagation in elastic media. Likewise, acoustic-wave modeling cannot yield any information about P- to S-wave mode conversion. Moreover, since isotropy is not a valid assumption for much of the Earth's subsurface, general seismic modeling and imaging techniques for anisotropic media needs to be developed. Virieux (1986), based on the first-order system of equations, applied conventional finite-differencing on a staggered grid to simulate P- and SV-wave propagation in elastic isotropic media. Faria and Stoffa (1994), also using the first-order system, performed finite-difference modeling in transversely isotropic media (with a vertical axis of symmetry) by a conventional fourth-order method.

Since finite-difference modeling and migration based on the full wave equation have none of the assumptions that limit solutions based on the one-way wave equation, the finite-difference method potentially can treat many issues accurately, such as arbitrary velocity variation, turning waves, and multiply reflected waves. This method, however, is costly when typical sampling intervals are used, placing heavy demands on computer memory and input/output devices (Reshef and Kessler, 1989; Blacquiere et al., 1989; Hale and Witte, 1992).

Unfortunately, conventional finite-difference schemes for numerically solving the wave equation suffer from undesirable ripples, so-called "grid dispersion" or "numerical dispersion," near large gradients in wavefields or when too coarse a computation grid is used. In their study of the numerical dispersion that arises in finite-difference methods, Alford et al. (1974) and Kelly et al. (1976) concluded that to eliminate the numerical

imposes no limitation on the range of reflector dips that can be accurately imaged.

$$w \equiv \frac{\partial P}{\partial z}, \tag{2.5}$$

the second-order acoustic wave equation (2.1) is reduced to the new first-order partial differential equation,

$$\frac{\partial q}{\partial t} = \frac{\partial}{\partial x}\left(\frac{u}{\rho}\right) + \frac{\partial}{\partial y}\left(\frac{v}{\rho}\right) + \frac{\partial}{\partial z}\left(\frac{w}{\rho}\right) + f. \tag{2.6}$$

Three additional first-order partial differential equations are derived from definitions (2.2) through (2.5); they are

$$\frac{\partial u}{\partial t} = \frac{\partial}{\partial x}\left(\rho c^2 q\right), \tag{2.7}$$

$$\frac{\partial v}{\partial t} = \frac{\partial}{\partial y}\left(\rho c^2 q\right), \tag{2.8}$$

$$\frac{\partial w}{\partial t} = \frac{\partial}{\partial z}\left(\rho c^2 q\right). \tag{2.9}$$

As in the hydrodynamics problem, the FCT correction can then be applied to these first-order equations. After applying the FCT to the first-order system, I found out that the FCT correction could readily be applied to the second-order wave equation, as well. Each of these two formulations has its particular merits.

2.2 Elastic media

For elastic media, the three general equations of motion are

$$\rho \frac{\partial^2 u_i}{\partial t^2} = f_i + \frac{\partial}{\partial x_j}\left(\sigma_{ij}\right) \qquad i = 1, 2, 3, \tag{2.10}$$

where x_1, x_2 and x_3 are the three Cartesian coordinates (later labeled x, y and z). u_i is displacement vector, ρ is density, f_i is the source function, and σ_{ij} are the components of the stress tensor. By Hooke's law, the stress and strain tensors satisfy $\sigma_{ij} = c_{ijpq} e_{pq}$, where c_{ijpq} are the elastic coefficients. The most general inhomogeneous anisotropic medium is defined by 21 independent components in c_{ijpq}, each of which can vary independently over space. e_{pq} are the components of the strain tensor

$$e_{pq} \equiv \frac{1}{2}\left(\frac{\partial u_p}{\partial x_q} + \frac{\partial u_q}{\partial x_p}\right). \tag{2.11}$$

Since the strain tensor is symmetric, it has six independent components: e_{11}, e_{22}, e_{33}, e_{12}, e_{13} and e_{23}.

With new dependent variables defined as

$$v_i \equiv \rho \frac{\partial u_i}{\partial t} \qquad i = 1, 2, 3, \tag{2.12}$$

and considering the six independent components of strain tensor e_{pq} as the other six

$$\sigma_{12} = 2C_{66}e_{12}, \tag{2.18}$$

where C_{11}, C_{33}, C_{44}, C_{13} and C_{66} are the five independent elastic coefficients that describe a general transversely isotropic (TI) medium, with axis of symmetry in the vertical (x_3) direction. With these strain and stress relations, the three equations of motion for transversely isotropic media, with vertical axis of symmetry, can be written as

$$\begin{aligned}\frac{\partial v_1}{\partial t} = f_1 \;+\; & \frac{\partial}{\partial x_1}\Big[C_{11}e_{11} + (C_{11} - 2C_{66})e_{22} + C_{13}e_{33}\Big] \\ & + \frac{\partial}{\partial x_2}\Big[2C_{66}e_{12}\Big] + \frac{\partial}{\partial x_3}\Big[2C_{44}e_{13}\Big],\end{aligned} \tag{2.19}$$

$$\begin{aligned}\frac{\partial v_2}{\partial t} = f_2 \;+\; & \frac{\partial}{\partial x_1}\Big[2C_{66}e_{12}\Big] + \frac{\partial}{\partial x_2}\Big[(C_{11} - 2C_{66})e_{11} + C_{11}e_{22} + C_{13}e_{33}\Big] \\ & + \frac{\partial}{\partial x_3}\Big[2C_{44}e_{23}\Big],\end{aligned} \tag{2.20}$$

$$\begin{aligned}\frac{\partial v_3}{\partial t} = f_3 \;+\; & \frac{\partial}{\partial x_1}\Big[2C_{44}e_{13}\Big] + \frac{\partial}{\partial x_2}\Big[2C_{44}e_{23}\Big] \\ & + \frac{\partial}{\partial x_3}\Big[C_{13}e_{11} + C_{13}e_{22} + C_{33}e_{33}\Big].\end{aligned} \tag{2.21}$$

Transversely isotropic media can be parametrized in any number of ways. Thomsen (1986) has developed a parametrization that is particular handy for understanding wave propagation in TI media. Using Thomsen parameters for TI media, the relations between the above elastic coefficients and Thomsen parameters are as follow,

$$\begin{aligned}\alpha_0 &\equiv \sqrt{\frac{C_{33}}{\rho}}, \\ \beta_0 &\equiv \sqrt{\frac{C_{44}}{\rho}}, \\ \varepsilon &\equiv \frac{C_{11} - C_{33}}{2C_{33}}, \\ \gamma &\equiv \frac{C_{66} - C_{44}}{2C_{44}}, \\ \delta &\equiv \frac{(C_{13} + C_{44})^2 - (C_{33} - C_{44})^2}{2C_{33}(C_{33} - C_{44})},\end{aligned} \tag{2.22}$$

where α_0 is P-wave velocity parallel to the symmetry axis, β_0 is S-wave velocity parallel to that axis, and ε, γ and δ are three dimensionless anisotropy parameters. With these relations, we can convert between the two sets of parameters.

Three first-order equations, (2.19) through (2.21), and six others, equations (2.14),

$$\frac{\partial e_{23}}{\partial t} = \frac{\partial}{\partial \tilde{x}_1}\left[\sin\theta\frac{v_2}{2\rho}\right] + \frac{\partial}{\partial \tilde{x}_3}\left[\cos\theta\frac{v_2}{2\rho}\right], \tag{2.30}$$

$$\frac{\partial e_{13}}{\partial t} = \frac{\partial}{\partial \tilde{x}_1}\left[\cos\theta\frac{v_3}{2\rho} + \sin\theta\frac{v_1}{2\rho}\right] + \frac{\partial}{\partial \tilde{x}_3}\left[-\sin\theta\frac{v_3}{2\rho} + \cos\theta\frac{v_1}{2\rho}\right]. \tag{2.31}$$

With equations (2.24) through (2.31), wave extrapolation in a TI medium with a tilted axis of symmetry can then be performed by the FCT finite-difference technique.

As with the acoustic case, the FCT technique is not just limited to the first-order system equations for elastic media, it can be applied to the second-order elastic wave equations (2.10) as well.

the Fourier modes (Potter, 1973)

$$u_j^{n+\frac{1}{2}} = \hat{u}^{n+\frac{1}{2}} e^{ikj\Delta x}, \tag{3.5}$$

$$q_j^{n+1} = \hat{q}^{n+1} e^{ikj\Delta x}. \tag{3.6}$$

Inserting these modes in equations (3.3) and (3.4), we get

$$\hat{u}^{n+\frac{1}{2}} = \hat{u}^{n-\frac{1}{2}} + \epsilon_1 2i \sin\left(\frac{1}{2}k\Delta x\right) \hat{q}^n, \tag{3.7}$$

$$\hat{q}^{n+1} = \hat{q}^n + \epsilon_2 2i \sin\left(\frac{1}{2}k\Delta x\right) \hat{u}^{n+\frac{1}{2}}. \tag{3.8}$$

From equations (3.7) and (3.8), we obtain the matrix equation

$$\begin{bmatrix} \hat{u}^{n+\frac{1}{2}} \\ \hat{q}^{n+1} \end{bmatrix} = \begin{bmatrix} 1 & 2i\epsilon_1 \sin\left(\frac{1}{2}k\Delta x\right) \\ 2i\epsilon_2 \sin\left(\frac{1}{2}k\Delta x\right) & 1 - 4\epsilon_1\epsilon_2 \sin^2\left(\frac{1}{2}k\Delta x\right) \end{bmatrix} \begin{bmatrix} \hat{u}^{n-\frac{1}{2}} \\ \hat{q}^n \end{bmatrix}. \tag{3.9}$$

The amplification matrix for this equation is

$$\mathbf{G} = \begin{bmatrix} 1 & 2i\epsilon_1 \sin\left(\frac{1}{2}k\Delta x\right) \\ 2i\epsilon_2 \sin\left(\frac{1}{2}k\Delta x\right) & 1 - 4\epsilon_1\epsilon_2 \sin^2\left(\frac{1}{2}k\Delta x\right) \end{bmatrix}, \tag{3.10}$$

for which the eigenvalues g satisfy

$$g^2 - 2\left[1 - 2\epsilon \sin^2\left(\frac{1}{2}k\Delta x\right)\right] g + 1 = 0, \tag{3.11}$$

where $\epsilon \equiv \left(\frac{c\Delta t}{\Delta x}\right)^2$. This equation gives two eigenvalues

$$g_{1,2} = 1 - 2\epsilon \sin^2\left(\frac{1}{2}k\Delta x\right) \pm 2\sqrt{\left[\epsilon \sin^2\left(\frac{1}{2}k\Delta x\right) - 1\right] \epsilon \sin^2\left(\frac{1}{2}k\Delta x\right)}. \tag{3.12}$$

If the above eigenvalues were real, then the magnitude $|g|$ of one eigenvalue would be greater than one; hence, the solution would be unstable. However, when the eigenvalues $g_{1,2}$ are complex, the magnitude $|g|$ of each eigenvalue is identically equal to unity. That is

$$|g| = 1 \qquad \text{iff } \left|\epsilon \sin^2\left(\tfrac{1}{2}k\Delta x\right)\right| \leq 1\,. \tag{3.13}$$

Thus if $\epsilon \leq 1$, solutions will be always stable. Hence, the stability condition for the leapfrog scheme is

$$\Delta t \leq \frac{\Delta x}{c}. \tag{3.14}$$

The dispersion relation for the finite-difference scheme defined by equations (3.3) and (3.4) can be obtained by relating the frequency ω of the Fourier mode on the grid

where, again, $\epsilon \equiv c^2(\Delta t/\Delta x)^2$. This dispersion relation equals the dispersion relation (3.18) for the differential equation only at low frequency, differing progressively more with increasing frequency.

By writing $\omega = \Omega + i\gamma$ ($\gamma \geq 0$), and equating the real and imaginary parts of the dispersion relation, we can analyze damping associated with individual frequency components (assuming k to be real), and get

$$\left(e^{\gamma\Delta t} - e^{-\gamma\Delta t}\right)\sin(\Omega\Delta t) = 0, \tag{3.24}$$

$$\left(e^{\gamma\Delta t} + e^{-\gamma\Delta t}\right)\cos(\Omega\Delta t) = 2 - 4\left(\frac{c\Delta t}{\Delta x}\right)^2 \sin^2\left(\frac{1}{2}k\Delta x\right). \tag{3.25}$$

From equations (3.24) and (3.25), we can first analyze the existence of numerical diffusion (or damping) in the finite-difference scheme. For frequencies satisfying $\sin(\Omega\Delta t) \neq 0$ [or $\cos(\Omega\Delta t) \neq \pm 1$], from equation (3.24) γ must be zero, which means no diffusion (or damping) on the grid occurs for these frequencies. For frequencies satisfying $\sin(\Omega\Delta t) = 0$, i.e., $\Omega = n\pi/\Delta t$ (n is an integer), there are two possibilities: (a) n is an even number, and (b) n is an odd number.

If n is even [i.e., $\cos(\Omega\Delta t) = 1$], equation (3.25) can then be rewritten as

$$\cosh(\gamma\Delta t) = 1 - 2\epsilon\sin^2\left(\frac{1}{2}k\Delta x\right). \tag{3.26}$$

Since $\cosh(\gamma\Delta t) \geq 1$ [$\cosh(\gamma\Delta t) = 1$, iff $\gamma = 0$] and the right hand side can be no greater than unity, this relation holds only for $\gamma = 0$ and for wavenumbers that satisfy $k = 2m\pi/\Delta x$ (m is an integer). So, in this case, no diffusion occurs.

If n is odd [i.e., $\cos(\Omega\Delta t) = -1$], equation (3.25) can be rewritten as

$$\cosh(\gamma\Delta t) + 1 = 2\epsilon\sin^2\left(\frac{1}{2}k\Delta x\right), \tag{3.27}$$

and, again, this relation holds only for $\gamma = 0$, and for certain wavenumbers and sampling choice ($\epsilon = 1$).

The above discussion suggests that the leapfrog is a non-diffusive finite-difference scheme, which has $\gamma = 0$ for each Fourier component. However, in the examples shown in Chapter 6, the leapfrog scheme does generate solutions with amplitude decay when a coarse grid is used. Clearly, the above analysis fails to characterize the damping that may exist for a given finite-difference scheme. The missing ingredient is the superposition of Fourier components having different phase speeds (the discussion of phase speed is in section 3 of this chapter). The amplitude of each Fourier component is unchanged during its propagation, and if the phase velocities for all the components are the same as the wave speed (i.e., no dispersion), the superposition does not cause any amplitude decay in the solution. This is the case for low-frequency wave propagation or when $\epsilon = 1$. However, if $\epsilon \neq 1$ and the propagating wave is not dominated by the low frequencies, due to the dispersion, the phase speeds for the various Fourier components differ from the

the same as for the leapfrog scheme.

Inserting equations (3.29) and (3.30), into (3.31) and (3.32), yields

$$q_j^{n+1} = q_j^n + \frac{\Delta t}{2\rho\Delta x}\left(u_{j+1}^n - u_{j-1}^n\right) + \frac{1}{2}\left(\frac{c\Delta t}{\Delta x}\right)^2\left(q_{j+1}^n - 2q_j^n + q_{j-1}^n\right), \tag{3.34}$$

$$u_j^{n+1} = u_j^n + \frac{\rho c^2\Delta t}{2\Delta x}\left(q_{j+1}^n - q_{j-1}^n\right) + \frac{1}{2}\left(\frac{c\Delta t}{\Delta x}\right)^2\left(u_{j+1}^n - 2u_j^n + u_{j-1}^n\right). \tag{3.35}$$

If we rewrite this difference form in the differential form to second-order accuracy, we obtain

$$\frac{\partial q}{\partial t} = \frac{1}{\rho}\frac{\partial u}{\partial x} + \frac{c^2\Delta t}{2}\frac{\partial^2 q}{\partial x^2}, \tag{3.36}$$

$$\frac{\partial u}{\partial t} = \rho c^2\frac{\partial q}{\partial x} + \frac{c^2\Delta t}{2}\frac{\partial^2 u}{\partial x^2}. \tag{3.37}$$

Note, in both equations (3.36) and (3.37), the second term on the right-hand side is the diffusion term introduced by the two-step Lax-Wendroff scheme. The diffusion coefficients in both are equal to $c^2\Delta t/2$.

To obtain the dispersion relation for this Lax-Wendroff scheme, we substitute Fourier modes (3.16) and (3.17) into equations (3.34) and (3.35), giving

$$\hat{q}e^{i\omega\Delta t} = \hat{q} - i\epsilon_1\hat{u}\sin(k\Delta x) + \epsilon\hat{q}[\cos(k\Delta x) - 1], \tag{3.38}$$

$$\hat{u}e^{i\omega\Delta t} = \hat{u} - i\epsilon_2\hat{q}\sin(k\Delta x) + \epsilon\hat{u}[\cos(k\Delta x) - 1]. \tag{3.39}$$

From the determinant of these two equations, we obtain the dispersion relation

$$e^{i\omega\Delta t} = 1 + \epsilon[\cos(k\Delta x) - 1] + i\sqrt{\epsilon}\sin(k\Delta x). \tag{3.40}$$

By writing $\omega = \Omega + i\gamma$, we again equate the real and imaginary parts of the dispersion relation,

$$\tan(\Omega\Delta t) = \frac{\sqrt{\epsilon}\sin(k\Delta x)}{1 + \epsilon[\cos(k\Delta x) - 1]}, \tag{3.41}$$

$$e^{-2\gamma\Delta t} = 1 - \epsilon(1 - \epsilon)[1 - \cos(k\Delta x)]^2, \tag{3.42}$$

where $\gamma \geq 0$.

In the special case where $\epsilon = 1$, γ is zero, and equation (3.41) becomes

$$\Omega = ck, \tag{3.43}$$

which is in precise agreement with the dispersion relation of the differential system.

In the low frequency limit, relation (3.41) becomes (3.43), and since we also have $\gamma = 0$ from (3.42), neither diffusion nor dispersion occurs. More generally, however, $\gamma > 0$ so that diffusion on the grid occurs (even without invoking superposition); furthermore, the phase velocity is a function of the wavenumber (again, this will be discussed in Section 3 of this chapter) so that dispersion occurs. Here, however, the presence of diffusion in

(3.37). Moreover, equation (3.50) has an added term in the third-order spatial derivative (higher-order diffusion). Because the diffusion coefficient in the pseudo Lax-Wendroff scheme is so much larger than that in the two-step Lax-Wendroff scheme and higher-order diffusion is introduced in solving u, I shall call the pseudo Lax-Wendroff scheme *strongly* diffusive.

To analyze the stability condition for the pseudo Lax-Wendroff scheme, we again use the Fourier modes

$$u_j^{n+1} = \hat{u}^{n+1} e^{ikj\Delta x}, \tag{3.51}$$

$$q_j^{n+1} = \hat{q}^{n+1} e^{ikj\Delta x}, \tag{3.52}$$

insert these modes in equations (3.47) and (3.46) to give

$$\hat{q}^{n+1} = \left[1 - 2\epsilon \sin^2\left(\frac{1}{2}k\Delta x\right)\right] \hat{q}^n + \epsilon_1 2i \sin\left(\frac{1}{2}k\Delta x\right) \hat{u}^n, \tag{3.53}$$

$$\hat{u}^{n+1} = \hat{u}^n + \epsilon_2 2i \sin\left(\frac{1}{2}k\Delta x\right) \hat{q}^{n+1}. \tag{3.54}$$

Substituting $\hat{q}^{n+1}$ into equation (3.54), we obtain

$$\begin{bmatrix} \hat{q}^{n+1} \\ \hat{u}^{n+1} \end{bmatrix} = \begin{bmatrix} 1 - 2\epsilon \sin^2\left(\frac{k\Delta x}{2}\right) & 2i\epsilon_1 \sin\left(\frac{k\Delta x}{2}\right) \\ 2i\epsilon_2 \sin\left(\frac{k\Delta x}{2}\right)\left[1 - 2\epsilon \sin^2\left(\frac{k\Delta x}{2}\right)\right] & 1 - 4\epsilon \sin^2\left(\frac{k\Delta x}{2}\right) \end{bmatrix} \begin{bmatrix} \hat{q}^n \\ \hat{u}^n \end{bmatrix}. \tag{3.55}$$

The amplification matrix for this equation is

$$\mathbf{G} = \begin{bmatrix} 1 - 2\epsilon \sin^2\left(\frac{1}{2}k\Delta x\right) & 2i\epsilon_1 \sin\left(\frac{1}{2}k\Delta x\right) \\ 2i\epsilon_2 \sin\left(\frac{1}{2}k\Delta x\right)\left[1 - 2\epsilon \sin^2\left(\frac{1}{2}k\Delta x\right)\right] & 1 - 4\epsilon \sin^2\left(\frac{1}{2}k\Delta x\right) \end{bmatrix}. \tag{3.56}$$

Its eigenvalues g satisfy

$$g^2 - 2\left[1 - 3\epsilon \sin^2\left(\frac{1}{2}k\Delta x\right)\right] g + 1 - 2\epsilon \sin^2\left(\frac{1}{2}k\Delta x\right) = 0, \tag{3.57}$$

which gives two eigenvalues

$$\begin{aligned} g_{1,2} &= 1 - 3\epsilon \sin^2\left(\frac{1}{2}k\Delta x\right) \\ &\pm \sqrt{\left[1 - 3\epsilon \sin^2\left(\frac{1}{2}k\Delta x\right)\right]^2 - \left[1 - 2\epsilon \sin^2\left(\frac{1}{2}k\Delta x\right)\right]} \\ &= 1 - 3\epsilon \sin^2\left(\frac{1}{2}k\Delta x\right) \pm \sqrt{\epsilon \sin^2\left(\frac{1}{2}k\Delta x\right)\left[9\epsilon \sin^2\left(\frac{1}{2}k\Delta x\right) - 4\right]}. \end{aligned} \tag{3.58}$$

If the eigenvalues are complex [i.e., $\epsilon \sin^2\left(\frac{1}{2}k\Delta x\right) \leq \frac{4}{9}$], the magnitude of each eigenvalue satisfies,

$$|g|^2 = 1 - 2\epsilon \sin^2\left(\frac{1}{2}k\Delta x\right) \leq 1. \tag{3.59}$$

Since $\epsilon \leq \frac{1}{2}$, this relation shows that wave-amplitude attenuation ($\gamma > 0$) always exists, even for the low-frequency limit. Moreover, since the dispersion relation of the pseudo Lax-Wendroff scheme differs from that of the differential equation, the phase velocity also differs from the true wave velocity, so numerical dispersion arises. Just as for the diffusive two-step Lax-Wendroff scheme, the added artificial diffusion in the pseudo Lax-Wendroff scheme is intended to help suppress the dispersive ripples.

3.2 Second-order system

Consider, now, the second-order acoustic wave equation in a one-dimensional homogeneous medium, which can be written as,

$$\frac{\partial^2 P}{\partial^2 t} = c^2 \frac{\partial^2 P}{\partial x^2}. \tag{3.70}$$

Equation (3.70) can then be approximated by the conventional finite-difference scheme, which has the form,

$$P_j^{n+1} = 2P_j^n - P_j^{n-1} + \epsilon(P_{j+1}^n - 2P_j^n + P_{j-1}^n), \tag{3.71}$$

where, again, $\epsilon \equiv \frac{c^2 \Delta t^2}{\Delta x^2}$, and the stability condition for this 1-D finite-difference scheme is again (Golub and Ortega, 1992)

$$\Delta t \leq \frac{\Delta x}{c}. \tag{3.72}$$

For a Fourier mode in time and space,

$$P(x,t) = \hat{P} e^{i(\omega t - kx)}, \tag{3.73}$$

as before the dispersion relation for wave equation (3.70) is

$$\omega^2 = c^2 k^2. \tag{3.74}$$

Again, as for the first-order differential equations, no damping of any mode occurs and all wavenumbers have the same velocity, so no dispersion occurs.

Applying the same Fourier mode (3.73) to the finite-difference scheme (3.71), and cancelling the common factors in the equation, yields

$$\sin^2\left(\frac{1}{2}\omega \Delta t\right) = \epsilon \sin^2\left(\frac{1}{2} k \Delta x\right). \tag{3.75}$$

This relation is the same as that for the leapfrog scheme, so that the discussion about the dispersion and diffusion is unchanged from that for the leapfrog scheme.

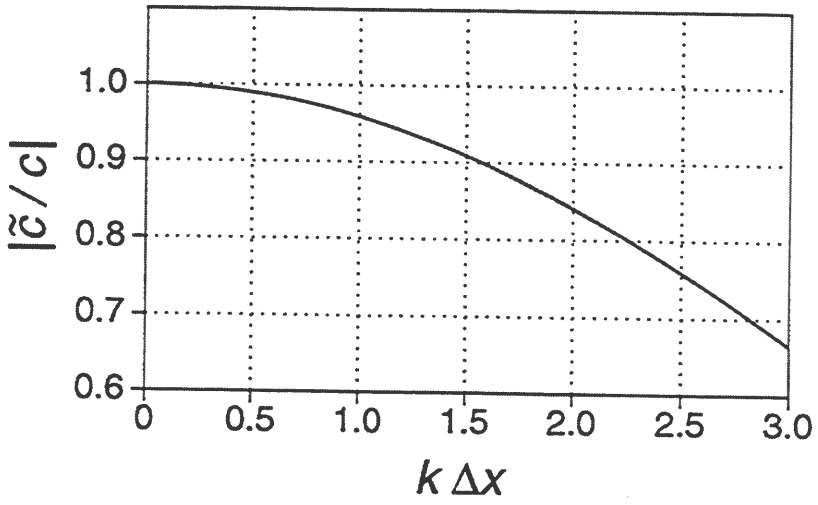

FIG. 3.1. Relative phase speed versus normalized wavenumber for spatial differencing in the leapfrog scheme.

arrival of true waves.

In the above analysis, we considered only the influence of spatial finite-differencing on the phase speed. Now, let us consider the influence of time differencing. Applying the finite-differencing to the time derivative only (as used in the leapfrog scheme) in equations (3.1) and (3.2), we have

$$u_{j+\frac{1}{2}}^{n+\frac{1}{2}} - u_{j+\frac{1}{2}}^{n-\frac{1}{2}} = \Delta t \rho c^2 \frac{\partial q}{\partial x}, \tag{3.83}$$

$$q_j^{n+1} - q_j^n = \frac{\Delta t}{\rho} \frac{\partial u}{\partial x}. \tag{3.84}$$

Substitution of the Fourier modes (3.16) and (3.17) into the equations (3.83) and (3.84) gives

$$\hat{u}\left[e^{\frac{1}{2}i\omega\Delta t} - e^{-\frac{1}{2}i\omega\Delta t}\right] = -i\Delta t \rho c^2 k \hat{q}, \tag{3.85}$$

$$\hat{u}\left[e^{\frac{1}{2}i\omega\Delta t} - e^{-\frac{1}{2}i\omega\Delta t}\right] = -i\frac{\Delta t}{\rho} k \hat{u}. \tag{3.86}$$

Combining the above two equations, we obtain

$$\frac{4\sin^2\left(\frac{1}{2}\omega\Delta t\right)}{\Delta t^2} = c^2 k^2. \tag{3.87}$$

With the phase speed defined in equation (3.81), we obtain the relative phase speed for

Lax-Wendroff scheme in the differential form

$$\frac{\partial q}{\partial t} = \frac{\Delta t}{2\rho\Delta x}\left(u_{j+1}^n - u_{j-1}^n\right) + \frac{1}{2}\left(\frac{c\Delta t}{\Delta x}\right)^2\left(q_{j+1}^n - 2q_j^n + q_{j-1}^n\right), \tag{3.89}$$

$$\frac{\partial u}{\partial t} = \frac{\rho c^2\Delta t}{2\Delta x}\left(q_{j+1}^n - q_{j-1}^n\right) + \frac{1}{2}\left(\frac{c\Delta t}{\Delta x}\right)^2\left(u_{j+1}^n - 2u_j^n + u_{j-1}^n\right). \tag{3.90}$$

Substituting the Fourier modes (3.16) and (3.17) into these equations, yields

$$i\omega\hat{q} = \frac{1}{\rho\Delta x}\left[-i\sin\left(k\Delta x\right)\right]\hat{u} + \frac{c^2\Delta t}{(\Delta x)}\left[\cos(k\Delta x) - 1\right]\hat{q}, \tag{3.91}$$

$$i\omega\hat{u} = \frac{\rho c^2}{\Delta x}\left[-i\sin\left(k\Delta x\right)\right]\hat{q} + \frac{c^2\Delta t}{(\Delta x)}\left[\cos(k\Delta x) - 1\right]\hat{u}. \tag{3.92}$$

Eliminating $\hat{u}$ and $\hat{q}$ from these equations, we obtain

$$\left\{i\omega - \frac{c^2\Delta t}{(\Delta x)}\left[\cos(k\Delta x) - 1\right]\right\}^2 = -\frac{c^2}{(\Delta x)^2}\sin^2\left(k\Delta x\right), \tag{3.93}$$

or

$$\omega = \frac{c}{\Delta x}\sin\left(k\Delta x\right) - i\frac{c^2\Delta t}{(\Delta x)^2}\left[\cos(k\Delta x) - 1\right]. \tag{3.94}$$

With the phase speed defined in equation (3.81), we obtain the relative phase speed for spatial differencing in the Lax-Wendroff scheme

$$\frac{\tilde{c}}{c} = \frac{\sin(k\Delta x)}{(k\Delta x)} - i\frac{c\Delta t}{k(\Delta x)^2}\left[\cos(k\Delta x) - 1\right], \tag{3.95}$$

a complex quantity reflecting the presence of diffusion. Thus, we have

$$\left|\frac{\tilde{c}}{c}\right| = \sqrt{\frac{\sin^2(k\Delta x)}{(k\Delta x)^2} + \frac{1}{(k\Delta x)^2}\left(\frac{c\Delta t}{\Delta x}\right)^2\left[\cos(k\Delta x) - 1\right]^2}. \tag{3.96}$$

Figure 3.3 shows relative phase speed versus normalized wavenumber for spatial differencing in the two-step Lax-Wendroff scheme. For this plot, I use a typical value of 0.64 for the parameter $\left(\frac{c\Delta t}{\Delta x}\right)^2$. As for the leapfrog scheme, wave speed is accurately computed for low frequencies, but decreases at an increasing rate as frequency increases. Comparing Figures 3.1 and 3.3, however, we see that the relative phase speed for the two-step Lax-Wendroff scheme changes more rapidly than does that of the leapfrog scheme, so the dispersion error of the two-step Lax-Wendroff scheme can be expected to be greater than that of the leapfrog scheme. However, in the two-step Lax-Wendroff scheme the artificial diffusion that is introduced helps to suppress some dispersion error.

To obtain the phase speed due to time differencing in the Lax-Wendroff scheme, we can follow procedures similar to those used in the analysis in the leapfrog scheme.

time differencing in the Lax-Wendroff scheme

$$\begin{aligned}\frac{\tilde{c}}{c} &= \frac{i\omega\Delta t}{e^{i\omega\Delta t}-1} \\ &= \frac{\omega\Delta t e^{-\frac{1}{2}i\omega\Delta t}}{2\sin\left(\frac{1}{2}\omega\Delta t\right)} \\ &= \frac{\omega\Delta t}{2\sin\left(\frac{1}{2}\omega\Delta t\right)}\left[\cos\left(\frac{1}{2}\omega\Delta t\right)-i\sin\left(\frac{1}{2}\omega\Delta t\right)\right].\end{aligned} \tag{3.103}$$

Thus, we have

$$\left|\frac{\tilde{c}}{c}\right| = \frac{\omega\Delta t}{2\sin\left(\frac{1}{2}\omega\Delta t\right)}. \tag{3.104}$$

Surprisingly, here, unlike the result for differencing in space, the relative phase speed for time differencing in the Lax-Wendroff scheme is identical to that of the leapfrog scheme [equation (3.88)]. Hence, the numerical dispersion caused by time discretization leads the true signal exactly as it did for the leapfrog scheme.

3.3.3 Pseudo Lax-Wendroff scheme

For the pseudo Lax-Wendroff scheme, we may rewrite equations (3.49) and (3.50), replacing the time differencing by a time derivative, so as to analyze the phase speed caused by spatial differencing. That is

$$\frac{\partial q}{\partial t} = \frac{1}{\rho\Delta x}\left(u^n_{j+1/2}-u^n_{j-1/2}\right)+\frac{1}{2}\frac{c^2\Delta t}{(\Delta x)^2}\left(q^n_{j+1}-2q^n_j+q^n_{j-1}\right), \tag{3.105}$$

$$\begin{aligned}\frac{\partial u}{\partial t} &= \frac{\rho c^2}{\Delta x}\left(q^n_{j+1}-q^n_j\right)+\frac{c^2\Delta t}{(\Delta x)^2}\left(u^n_{j+3/2}-2u^n_{j+1/2}+u^n_{j-1/2}\right) \\ &+ \frac{\rho c^2}{2\Delta x}\left(\frac{c\Delta t}{\Delta x}\right)^2\left(q^n_{j+2}-3q^n_{j+1}+3q^n_j-q^n_{j-1}\right).\end{aligned} \tag{3.106}$$

With the Fourier modes (3.16) and (3.17), we obtain

$$i\omega\hat{q} = \frac{-2i}{\rho\Delta x}\sin\left(\frac{1}{2}k\Delta x\right)\hat{u}-\frac{2c^2\Delta t}{(\Delta x)^2}\sin^2\left(\frac{1}{2}k\Delta x\right)\hat{q}, \tag{3.107}$$

$$\begin{aligned}i\omega\hat{u} &= \frac{-2i\rho c^2}{\Delta x}\sin\left(\frac{1}{2}k\Delta x\right)\hat{q}-\frac{4c^2\Delta t}{(\Delta x)^2}\sin^2\left(\frac{1}{2}k\Delta x\right)\hat{u} \\ &+ \frac{4i\rho c^2}{\Delta x}\left(\frac{c\Delta t}{\Delta x}\right)^2\sin^3\left(\frac{1}{2}k\Delta x\right)\hat{q}.\end{aligned} \tag{3.108}$$

that in the two-step Lax-Wendroff scheme) will reduce some of the dispersive ripple. Therefore, the pseudo Lax-Wendroff scheme should perform better than the two-step Lax-Wendroff scheme in suppressing numerical dispersion.

For the pseudo Lax-Wendroff scheme, as with the leapfrog and Lax-Wendroff schemes, the time differencing also influences the phase speed. We could follow the same procedures for the Lax-Wendroff scheme to analyze the phase speed due to time differencing in the pseudo Lax-Wendroff scheme. However, since time differencing in the Lax-Wendroff and pseudo Lax-Wendroff schemes are both computed from data at time steps n and $n+1$, the influence of time differencing on the phase speed should be the same, and I find that to be the case.

3.3.4 Second-order conventional scheme

If we apply second-order finite-differencing to the spatial derivative in equation (3.70), the finite-difference scheme has the form

$$\frac{\partial^2 P}{\partial t^2} = \frac{c^2}{\Delta x^2}(P_{j+1}^n - 2P_j^n + P_{j-1}^n). \tag{3.116}$$

Substitution of the Fourier mode (3.73) into equation (3.116) gives

$$-\omega^2 = \frac{2c^2}{\Delta x^2}[\cos(k\Delta x) - 1]. \tag{3.117}$$

Using the definition of the phase speed, equation (3.81), we obtain the relative phase speed

$$\frac{\tilde{c}}{c} = \frac{2\sin\left(\frac{1}{2}k\Delta x\right)}{(k\Delta x)}. \tag{3.118}$$

Not surprising, this expression is identical to that for the leapfrog scheme applied to the system of first-order equations. Again, however, this approach lacks the artificial diffusion of the pseudo Lax-Wendroff scheme and thus has no ability to suppress the dispersion.

Now, consider time-differencing alone. Applying the second-order finite-differencing to the time derivative only, in equation (3.70), we have

$$P_j^{n+1} - 2P_j^n + P_j^{n-1} = c^2\frac{\partial^2 P}{\partial x^2}. \tag{3.119}$$

Substitution of the Fourier mode (3.73) into equation (3.119) yields

$$\frac{2[\cos(\omega\Delta t) - 1]}{\Delta t^2} = -c^2k^2. \tag{3.120}$$

Chapter 4

ANALYSIS OF FLUX-CORRECTED TRANSPORT

In this chapter, I give a detailed discussion about the flux-corrected transport technique, and show how the artificial diffusion and anti-diffusion in the FCT method work. I also discuss how the use of diffusion and anti-diffusion in the FCT algorithm alters the dispersion relationship for the first-order system. A comparable argument applies to the second-order system.

Broadly, the FCT technique consists of two major stages — a conventional finite-difference stage (Stage I), followed by a correction stage (Stage II) which consists of *diffusion* and *anti-diffusion* steps applied throughout the evolution of the computed wavefield. In the correction stage the computed wavefield is modified so as to suppress the artificial ripples caused by the numerical dispersion. The idea of modifying the calculations to improve the solution is not new. In the Lax-Wendroff scheme (Lax and Wendroff, 1960) a certain degree of diffusion is introduced into the finite-difference equations to suppress the grid dispersion. Solutions of the wave equations obtained by the Lax-Wendroff method, unfortunately, suffer smoothing and a loss of resolution throughout, primarily because the diffusion is too heavy-handed an approach to curing the dispersion problem, and, moreover, a certain amount of dispersion remains. As the numerical dispersion does not arise everywhere on the computational grid at every time step, it would be desirable if application of the smoothing procedure could be limited to just where and when it is need.

This idea is the essence of philosophy underlying the FCT technique. Appendices B and C give recipes for the FCT correction procedure associated with solution of the first-order and second-order systems of wave equations for 3-D media. In practice, there is no a priori information about where the dispersion actually exists. Therefore, the FCT method first applies the diffusion everywhere at each time step (steps 2 and 4 in Appendices B and C). Once the solution is diffused for the given time step, an opposing anti-diffusion is introduced at that time step to counteract the diffusion wherever it *seems* not to be needed (steps 3, 5 and 6 in Appendices B and C). Because it is applied selectively to various portions of the data, this anti-diffusion step is a non-linear procedure.

Before I give a detailed discussion of the FCT algorithm, let us briefly review the FCT correction procedure for the simple 1-D problem. The FCT method for the first-order system for acoustic wave extrapolation proceeds as follows:

1. Advance the solutions by a standard finite-difference method, say the leapfrog method, for example.

2. Compute *diffusive fluxes* at time level n, then use these fluxes in step 4 to diffuse

As we shall see, the nonlinear step, equation (4.6), involves decision-making to assess where numerical diffusion seems not to have occurred in the original finite-differencing.

The algorithm listed above involves three major operations, conventional finite-difference (i.e. transport), diffusion and anti-diffusion, which can be symbolically represented as $\mathbf{T}$, $\mathbf{D}$ and $\mathbf{A}$, respectively. Also, let $\mathbf{I}$ represent the identity operator. Operators $\mathbf{T}$ and $\mathbf{D}$ are linear. However, because it operates only locally, based on a search for local extrema, operator $\mathbf{A}$ is nonlinear. The old values of $\{q_j^n\}$ $(j = 1, 2, \cdots, J)$ and $\{u_{j+1/2}^{n+1/2}\}$ $(j = 1, 2, \cdots, J-1)$ in the leapfrog scheme are carried by $\mathbf{I}$ and $\mathbf{T}$, respectively, into new values $\{q_j^T\}$, and then are subsequently diffused to become $\{q_j^{TD}\}$. After anti-diffusion, $\{q_j^{TD}\}$ produces the corrected values $\{q_j^{n+1}\}$ at the new time step. Symbolically, the FCT sequence can be represented as

$$q^T = q^n + \mathbf{T}u^{n+\frac{1}{2}}, \tag{4.7}$$

$$q^{TD} = q^T + \mathbf{D}q^n, \tag{4.8}$$

$$q^{n+1} = q^{TD} + \mathbf{A}\{q^T, q^{TD}\}. \tag{4.9}$$

Here, equation (4.7) is based on equation (3.4), and equation (4.8) on equation (4.3). Specifically, for the leapfrog scheme the operators $\mathbf{T}$ and $\mathbf{D}$ have the matrix forms

$$\mathbf{T}^{J\times(J-1)} = \begin{bmatrix} \alpha & & & & & \\ -\epsilon_2 & \epsilon_2 & & & 0 & \\ & -\epsilon_2 & \epsilon_2 & & & \\ & & \cdot & \cdot & & \\ & & & \cdot & \cdot & \\ & & & & \cdot & \cdot \\ & 0 & & & -\epsilon_2 & \epsilon_2 \\ & & & & & \beta \end{bmatrix}, \tag{4.10}$$

$$\mathbf{D}^{J\times J} = \begin{bmatrix} \alpha_1 & \beta_1 & & & & & \\ \eta_1 & -2\eta_1 & \eta_1 & & & 0 & \\ & \eta_1 & -2\eta_1 & \eta_1 & & & \\ & & \cdot & \cdot & \cdot & & \\ & & & \cdot & \cdot & \cdot & \\ & & & & \cdot & \cdot & \cdot \\ & 0 & & & \eta_1 & -2\eta_1 & \eta_1 \\ & & & & & \beta_2 & \alpha_2 \end{bmatrix}, \tag{4.11}$$

where, $\epsilon_2 \equiv \Delta/\rho\Delta x$, and α, β, α_1, β_1, α_2 and β_2 are coefficients related to the boundary conditions.

The order of the operations that carry q^n into q^{n+1} is important; the operations do not commute in general.

then the result of this anti-diffusion would be

$$\begin{aligned}\frac{q_j^{DA}}{q_j^n} &= \frac{(1+2\eta)q_j^D - \eta(q_{j+1}^D + q_{j-1}^D)}{q_j^n} \\ &= \{1-2\eta[\cos(k\Delta x)-1]\}\{1+2\eta[\cos(k\Delta x)-1]\} \\ &= 1-4\eta^2[\cos(k\Delta x)-1]^2 \leq 1. \end{aligned} \tag{4.17}$$

Here, $\{1-2\eta[\cos(k\Delta x)-1]\} \geq 1$ is an amplifying factor introduced by anti-diffusion. The net action of diffusion and anti-diffusion, as indicated in equation (4.17), however, is a residual diffusion (amplitude ratio is ≤ 1). Thus, the net result is some amplitude loss. To minimize this amplitude loss, we might like the anti-diffusive flux to be defined other than by equation (4.16).

If the anti-diffusive flux instead were given by

$$\tilde{f}_{j+1/2} \equiv \eta(q_{j+1}^n - q_j^n), \tag{4.18}$$

rather than in terms of the diffused values q^D, anti-diffusion would cancel the diffusion exactly, and would give back the original undiffused solution; that is,

$$q_j^{DA} = q_j^D - \tilde{f}_{j+1/2} + \tilde{f}_{j-1/2} = q_j^n. \tag{4.19}$$

To soften the loss of amplitude, we would therefore like the anti-diffusion to have an action given either by equation (4.16) or by equation (4.18), but only for the area where anti-diffusion is needed. For the true wavefield (i.e., with no numerical dispersion), we would want the anti-diffusive flux to be defined as (4.18), so it can cancel the diffusion exactly. In contrast, for the approximate, computed wavefield (which has some minor numerical dispersion), the anti-diffusive flux defined in (4.16) might be a good choice, since the amount of residual diffusion (net effect of the diffusion and anti-diffusion steps) might be sufficient to suppress the minor dispersion error.

When $\mathbf{T}$ is not vanishing, we might define the anti-diffusive flux, $\tilde{f}_{j+\frac{1}{2}}$, such that $\tilde{f}_{j+\frac{1}{2}}$ reduces to equation (4.18) when $\mathbf{T}$ vanishes. With such a definition, the FCT-corrected solution [equation (4.9)] becomes

$$q_j^{n+1} = q_j^{TD} - \tilde{f}_{j+1/2} + \tilde{f}_{j-1/2}, \tag{4.20}$$

where q_j^{TD} is obtained from equations (4.7) and (4.8), and the anti-diffusive flux is given by

$$\tilde{f}_{j+1/2} \equiv \eta(q_{j+1}^T - q_j^T). \tag{4.21}$$

For non-vanishing operation $\mathbf{T}$, the Fourier mode of u in time and space is

$$u = \hat{u}e^{i(\omega t - kx)}. \tag{4.22}$$

From the definitions of q [equation (2.2)] and u [equation (2.3)], and relation (4.14), the

4.2 Selectively applied anti-diffusive fluxes

Consider the situation depicted in Figure 4.1, which shows, schematically, a wavefield snapshot generated by conventional finite-differencing in a coarsely sampled 1-D medium. The wave is propagating to the right with a constant velocity c. During propagation, restricted regions of the computed wavefield are presumed to suffer from high-frequency numerical dispersion and other regions not, as indicated in the figure. In this simplistic depiction, the lower-frequency portion of the computed wavefield corresponds the true data, while the near-Nyquist-frequency portion corresponds to the numerical dispersion attributable to coarse sampling. The FCT correction, ideally, would keep the true signal (non-dispersive portion of the wavefield) unchanged while it suppresses the numerical dispersion.

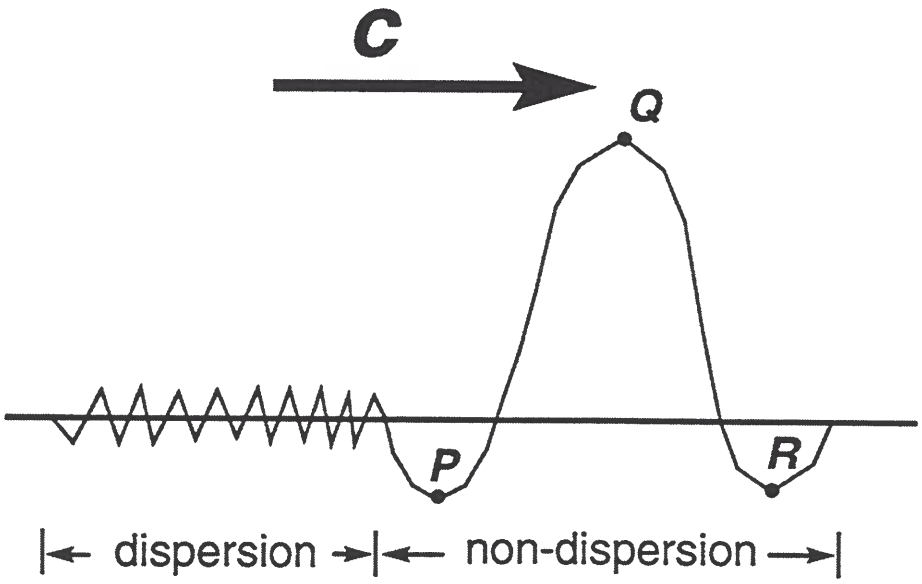

FIG. 4.1. Schematic snapshot of 1-D wavefield depicting regions of dispersive ripples and non-dispersive true wavefield.

In the FCT approach, the key assumption in deciding where the anti-diffusion is needed is that all local extrema (in the unsmoothed solution) are caused by numerical dispersion. Based on this assumption, the anti-diffusion is applied only over portions where there are no local extrema. That is, the anti-diffusive flux, computed at every half grid point $j + 1/2$ in equation (4.26), should act at adjacent points j and $j + 1$ only if no local extrema exist at these two positions. Figure 4.2 illustrates four situations where the data amplitudes either do or do not show local extrema at spatial positions j or $j+1$, for the situation of a positive slope between the two positions. For case (a) in Figure 4.2, there is no local extremum at either j or $j + 1$; however, for cases (b), (c) and (d), local extrema are present at either j or $j + 1$, or at both.

the algorithm is based on the simplistic and incorrect premise that local extrema are indicative of numerical dispersion, no anti-diffusion will be applied at these three points after the diffusion step. Therefore, any amplitude loss introduced by the diffusion stage will not be compensated during the current time step at these points. After the FCT correction at the current time step, however, the points adjacent to P, Q and R might become the new local extrema, hence, the anti-diffusion might be applied to P, Q and R points at the next time step. The net action after many recursions is that the real features are not reduced as much as is the numerical dispersion. As we shall see in the data examples, below, this is indeed the case.

4.3 Anti-diffusion for a strongly diffusive, finite-difference scheme

In the conventional stage (i.e., first stage) of the FCT method, one might use a strongly diffusive finite-difference scheme (such as pseudo Lax-Wendroff) to advance the solution in order to reduce numerical dispersion, at the price of some amplitude and resolution losses. In this situation, we would not need the smoothing (or diffusion) procedure in the FCT method, and need apply only the anti-diffusion correction to the solution in order to compensate the amplitude and resolution losses introduced in the conventional finite-differencing stage.

Alternatively, if we follow the leapfrog scheme [equations (3.3) and (3.4)] with just the diffusion stage [equation (4.3)] in the FCT method, we would have

$$q_j^{n+1} = q_j^n + \frac{\Delta t}{\rho \Delta x}\left(u_{j+1/2}^n - u_{j-1/2}^n\right) + \eta_1\left(q_{j+1}^n - 2q_j^n + q_{j-1}^n\right). \tag{4.30}$$

Comparing this equation with the pseudo Lax-Wendroff scheme for solving variable q [equation (3.47)], we see that a difference between the two is that in the pseudo Lax-Wendroff scheme [equation (3.47)], the diffusion coefficient is fixed at $\eta_1 = (c\Delta t/\Delta x)^2/2$, whereas in the FCT diffusion step, η_1 can be chosen differently. Another difference between the leapfrog approach with the FCT diffusion step and the pseudo Lax-Wendroff method is in the computation of the variable u [compare equations (3.3) and (3.48)].

From this analysis, we expect similarities between the actions of a strongly diffusive finite-difference scheme, such as the pseudo Lax-Wendroff, and the leapfrog scheme with the FCT diffusion correction. Therefore, as mentioned above when combining the FCT technique with a strongly diffusive finite-difference scheme, the diffusion-correction stage is not necessary. To compensate the resolution and amplitude losses that are introduced by the strongly diffusive finite-difference scheme, we need only use the anti-diffusion correction. We can do this by simply choosing η_1 to be zero and η_2 to be nonzero. However, this is not an efficient approach, since the diffusion correction (with zero values) would unnecessarily be applied throughout. An efficient approach, which ignores the diffusion correction and applies only the anti-diffusion correction, is given in Chapter 5.

4. Modify (i.e. *diffuse* locally) the solution q using the localized diffusive fluxes f^c and obtain the corrected solution; this process smooths the solution only where numerical dispersion is thought to exist:

$$q_j^{n+1} = q_j^{n+1} + ({f^c}_{j+1/2} - {f^c}_{j-1/2}). \tag{5.5}$$

Generalization of the optimized FCT localized diffusion correction procedures to the three-dimensional problem based on the first-order system equations and the original second-order wave equation is given in Appendices D and E, respectively. Since the optimized FCT correction involves only the localized diffusion, it saves about 40 percent computational cost compared with that of the correction portion of the FCT procedure discussed in Chapter 4.

If, in the conventional stage, a strongly diffusive scheme, such as the pseudo Lax-Wendroff scheme, is used, the diffusion stage in the full FCT procedure becomes unnecessary. We can optimize the FCT procedure for the strongly diffusive scheme as well. The anti-diffusion correction for the first-order system proceeds as follows:

1. Advance the solutions by a strongly diffusive finite-difference method.

2. Compute *anti-diffusive fluxes* at time level n:

$$f_{j+1/2} = \eta(q_{j+1}^n - q_j^n), \tag{5.6}$$

where η is an anti-diffusion coefficient (depending on the diffusion coefficient in the strongly diffusive finite-difference stage), which can be chosen much as for η_2 in equation (4.2). Typically, the value can be a few percent larger than the fixed value of the diffusion coefficient in the strongly diffusive finite-difference scheme.

3. Compute the corrected anti-diffusive fluxes:

$${f^c}_{j+1/2} = \frac{1}{2} f_{j+1/2} \left[\text{sign}(f_{j+1/2} f_{j-1/2}) + \text{sign}(f_{j+1/2} f_{j+3/2}) \right]. \tag{5.7}$$

4. Modify (i.e. *anti-diffuse* locally) the solution q using the localized anti-diffusive fluxes f^c to obtain the corrected solution:

$$q_j^{n+1} = q_j^{n+1} - ({f^c}_{j+1/2} - {f^c}_{j-1/2}). \tag{5.8}$$

This optimized anti-diffusion correction can be generalized to three-dimensional problems for both the first-order and second-order system equations, just as can the full FCT procedure. Similar to the optimized FCT localized diffusion, this optimized FCT anti-diffusion correction also promises about 40 percent saving compared with the computational effort of the full FCT correction procedure (disregarding the cost of the conventional finite-differencing).

In the next chapter, we shall see the action of these various approaches to suppressing numerical dispersion, study the dependence of solutions on values for η_1 and η_2 (or η),

Chapter 6

APPLICATION TO ACOUSTIC MEDIA

I have tested the FCT correction on one-dimensional forward problems, two-dimensional modeling and reverse-time depth migration, and three-dimensional modeling. The reverse-time depth migration, which is basically the same as forward modeling, simply runs time backwards.

For the one-dimensional case, the wave is propagating along the z-axis, so $\frac{\partial}{\partial x} = \frac{\partial}{\partial y} = 0$. Forward modeling tests involve a wavelet that is an isolated full-cycle of a sinusoid, $0.5\cos(2\pi ft)+0.5$. Tests are also carried out for isolated rectangular pulses. The medium is homogeneous in these tests, and the FCT algorithms used are based on the first-order partial differential equations.

For the two-dimensional case where $\frac{\partial}{\partial y} = 0$, I present tests of both modeling and migration with FCT correction based on both the first-order partial differential equations and the second-order wave equation.

The three-dimensional modeling tests are performed in a homogeneous medium, and the FCT correction is based on the second-order wave equation.

6.1 First-order system

In this section, I present results of FCT-corrected 1-D modeling, 2-D migration impulse response results, and migration imaging for a reflector model. Here, the FCT correction is based on the first-order acoustic wave equations.

6.1.1 One-dimensional modeling tests

In the one-dimensional modeling tests, I consider transmitted waves only, and the medium has a constant density and a constant velocity of 2 km/s. In each of the modeling tests, I specify a time sequence at the surface and examine a snapshot of the generated wavefield in depth. We shall see how choices of the diffusion coefficients η_1 and η_2 in the full FCT approach and η in the optimized approach govern the quality of the modeling results.

Rectangular pulses — Figure 6.1 shows the snapshots at time t =1 s for three isolated rectangle-function pulses at the surface 0.333 s apart. The spatial step is 0.01 km, and the number of grid points per pulse width is eight. This test is extreme in that the waveform is discontinuous in time and therefore in space.

Ideally, the waveform would not change during its propagation down through the homogeneous earth; that is, as shown in Figure 6.1a, the waveform would remain as a sequence of rectangular pulses. When using the leapfrog finite-difference method, however,

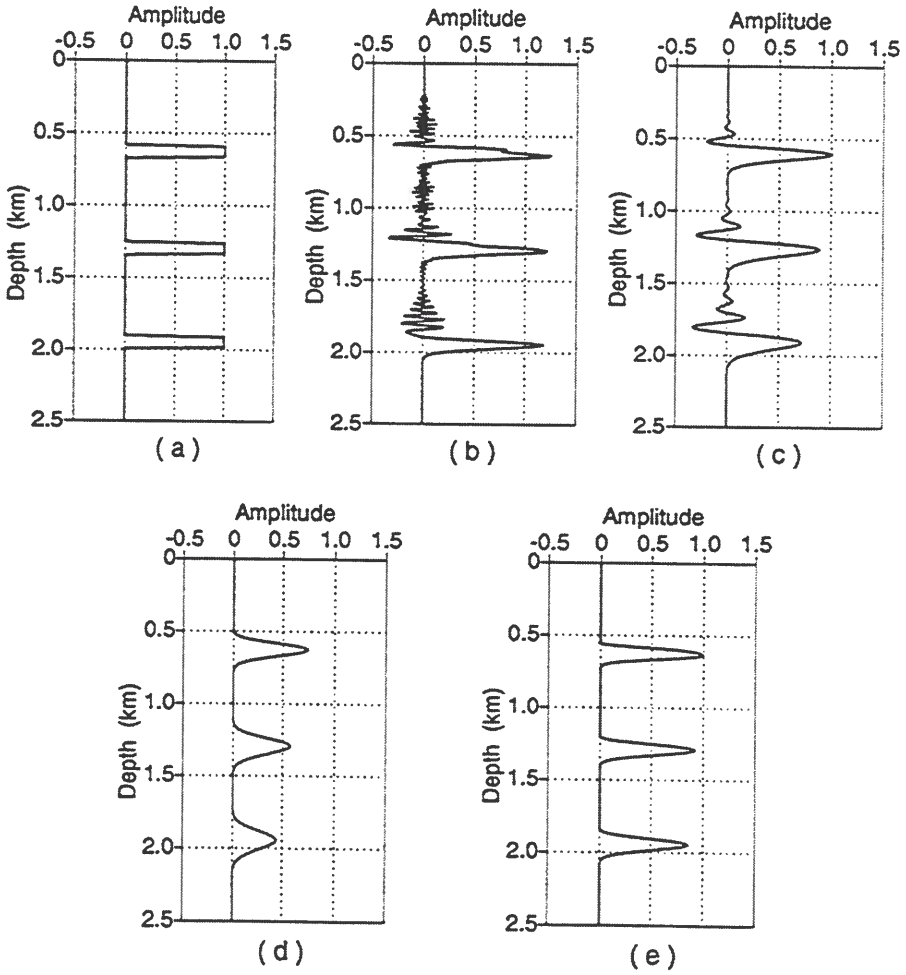

FIG. 6.1. Snapshot from a one-dimensional modeling test for isolated rectangular pulses (eight samples per pulse width), for a constant velocity of 2 km/s and a constant density. (a) Ideal wavefield. (b) Wavefield obtained by the leapfrog finite-difference scheme. (c) Wavefield obtained by the two-step Lax-Wendroff finite-difference scheme. (d) Wavefield obtained by the pseudo Lax-Wendroff finite-difference scheme. (e) Wavefield obtained by the leapfrog scheme with the FCT diffusion correction only.

larger than those used to obtain Figure 6.2a. Even though solution shows removal of the numerical dispersion, the waveforms, are more distorted than those in Figure 6.2a. Despite the distortions in Figures 6.3a and 6.3b, the solutions for this wide range of η_1 and η_2 values are considerably superior to those generated by conventional (i.e., no FCT correction) schemes.

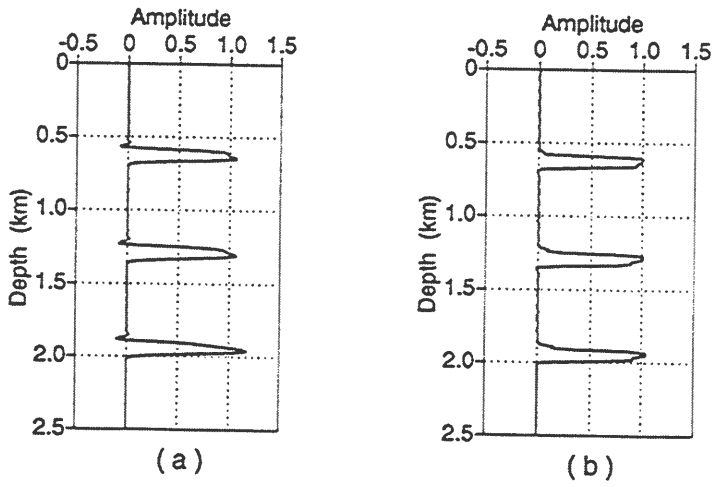

FIG. 6.3. More snapshots from the one-dimensional modeling test with rectangular pulses. (a) Wavefield obtained by the leapfrog scheme with the full FCT diffusion and anti-diffusion corrections ($\eta_1 = 0.026$; $\eta_2 = 0.027$). (b) Wavefield obtained by the leapfrog scheme with the full FCT diffusion and anti-diffusion corrections ($\eta_1 = 0.042$; $\eta_2 = 0.046$).

With the optimized FCT correction, Figure 6.4 shows wavefield snapshots for two different values of η: $\eta = 0.09$ in Figure 6.4a, and $\eta = 0.15$ in Figure 6.4b, 25 percent less than and larger than that used in Figure 6.2c, respectively. Although none of the solutions with the optimized approach are as crisp as the best result for the full FCT approach, they nevertheless are quite good. Use of too low a value of η leaves a precursor in the pulses, while use of too large a value causes too much smoothing.

From these examples with different choices of parameters η_1, η_2 and η, we see that while the values of η_1, η_2 and η do influence the quality of the solutions, the choices need not be precise.

Sinusoid pulses — Figures 6.5 through 6.7 show snapshots at time $t = 1$ s, generated by three isolated sinusoids (dominant frequency of 10 Hz) 0.333 s apart at the surface. The spatial steps are 0.01 km (twenty samples per dominant wavelength), 0.025 km (eight samples per dominant wavelength) and 0.04 km (five samples per dominant wavelength), respectively.

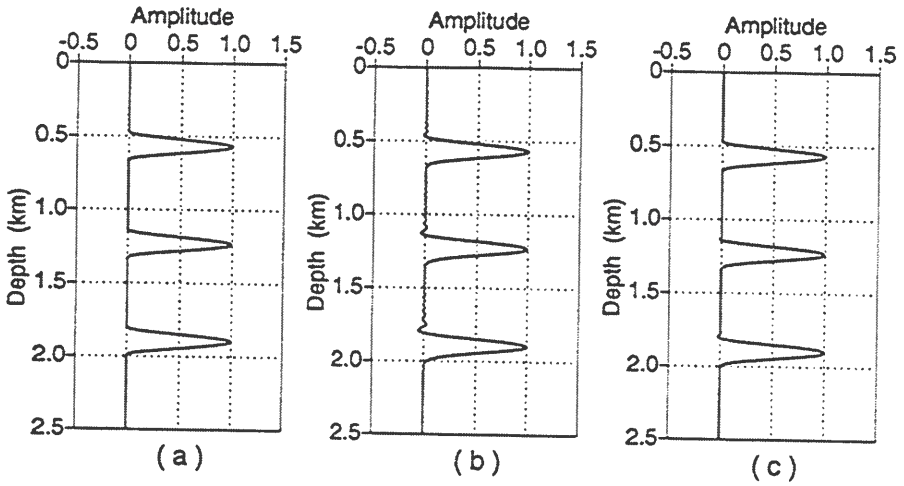

FIG. 6.5. One-dimensional test for isolated wavelets, each of which is a full-cycle of a sinusoid with a frequency of 10 Hz, for a constant velocity of 2 km/s and a constant density. The spatial step is $\Delta x = 0.01$ km (twenty samples per dominant wavelength). (a) Ideal wavefield. (b) Wavefield obtained by the standard leapfrog finite-difference method. (c) Wavefield obtained with the full FCT correction.

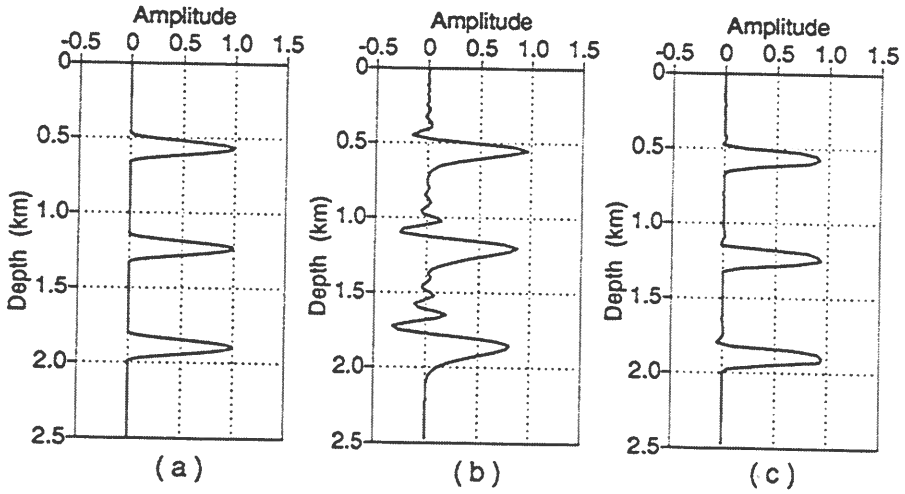

FIG. 6.6. Same as Figure 6.5, except $\Delta x = 0.025$ km (eight samples per dominant wavelength).

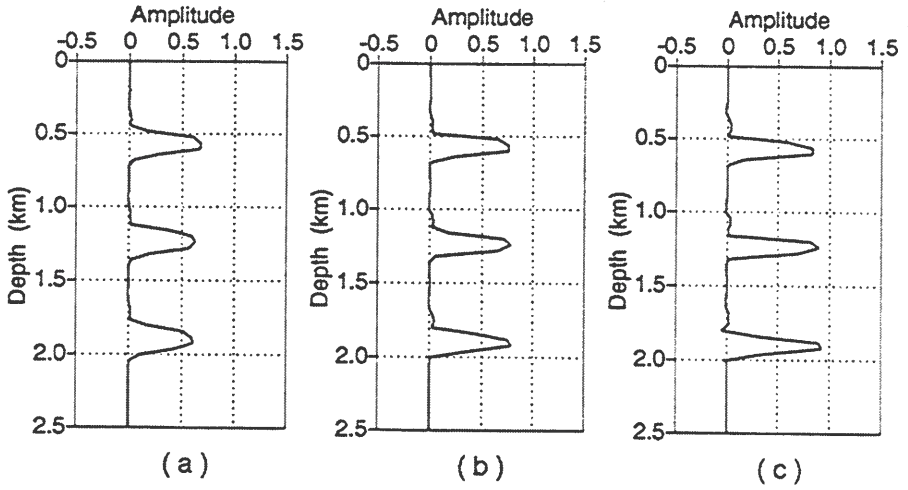

FIG. 6.8. Comparison of the wavefield snapshot generated by the leapfrog method with the FCT correction for a fixed diffusion coefficient ($\eta_1 = 0.042$) and differing η_2 on a vary coarse grid ($\Delta x = 0.04$ km, five samples per dominant wavelength). (a) $\eta_2 = 0.052$, (b) $\eta_2 = 0.072$, and (c) $\eta_2 = 0.092$.

has a velocity of 2.0 km/s and a constant density. For the step sizes, $\Delta x = \Delta z = 0.02$ km, the number of grid points per upper half-power wavelength (G_0) is about 3.5 (a coarse grid). The time step used in the tests here is 4 ms.

Figures 6.9 and 6.10 show the finite-difference solutions by the leapfrog scheme without and with the FCT correction. Without the full FCT correction, the leapfrog solution for the coarse grid shows strong numerical dispersion, as well as progressive loss of resolution with increasing depth of scatters (Figure 6.9). With the full FCT diffusion and anti-diffusion correction ($\eta_1 = 0.05$; $\eta_2 = 0.05$; Figure 6.10), the numerical dispersion has been suppressed and the resolution loss has been largely restored.

Similar to the 1-D examples, the optimized FCT approach applied to the leapfrog solution ($\eta = 0.08$) also yields a solution without numerical dispersion and restores much of the lost resolution (Figure 6.11), but not so completely as in Figure 6.10.

To see the dependence of the quality of the solutions on the parameters η_1 and η_2 for the full FCT correction, I, again, choose values that are either 25 percent less or 25 percent larger than those values used in Figure 6.10.

First, I show examples in which η_1 and η_2 change together. In Figure 6.12, with $\eta_1 = 0.038$ and $\eta_2 = 0.038$ (about 25 percent less than those used in Figure 6.10), the leapfrog scheme with the full FCT correction produces a solution with most of the dispersive ripples removed. Moreover, the solution appears as though it has undergone a phase change. This appearance is, in fact, due to a residual precursor that is not fully removed by the FCT diffusion, since the artificial diffusion introduced here is less than that in Figure 6.10. Parameters of $\eta_1 = 0.062$ and $\eta_2 = 0.062$ (Figure 6.13) result in

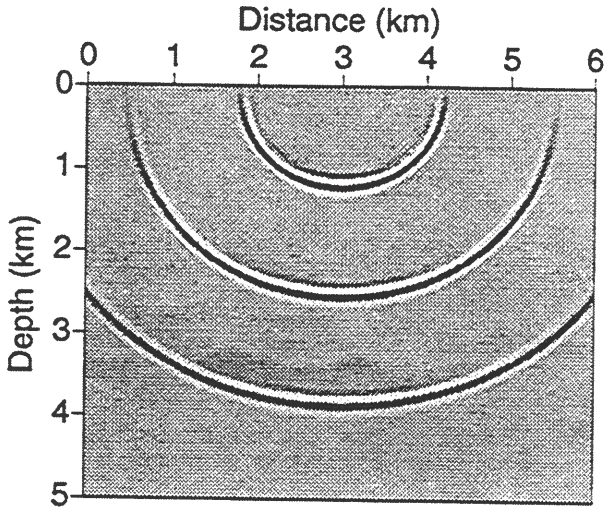

FIG. 6.10. Migration impulse responses by the leapfrog finite-difference method with the full FCT correction ($\eta_1 = 0.05$; $\eta_2 = 0.05$).

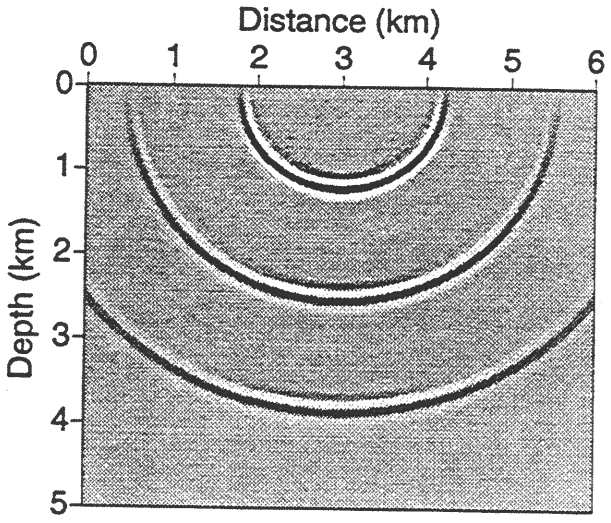

FIG. 6.11. Migration impulse responses by the leapfrog finite-difference method with the optimized FCT (localized diffusion) correction ($\eta = 0.08$).

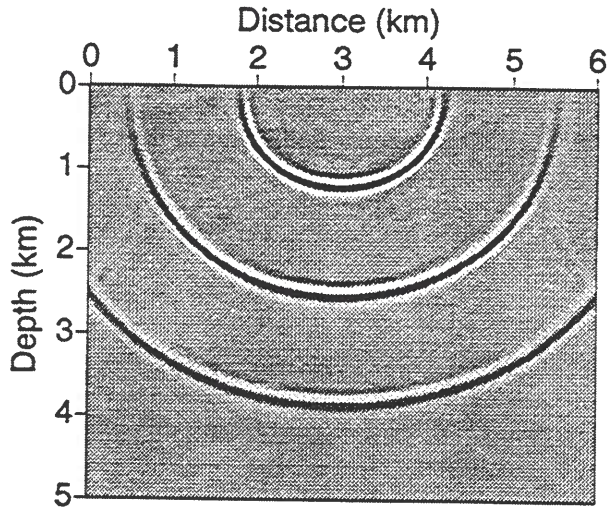

FIG. 6.14. Migration impulse responses by the leapfrog finite-difference method with the full FCT correction ($\eta_1 = 0.05$; $\eta_2 = 0.038$).

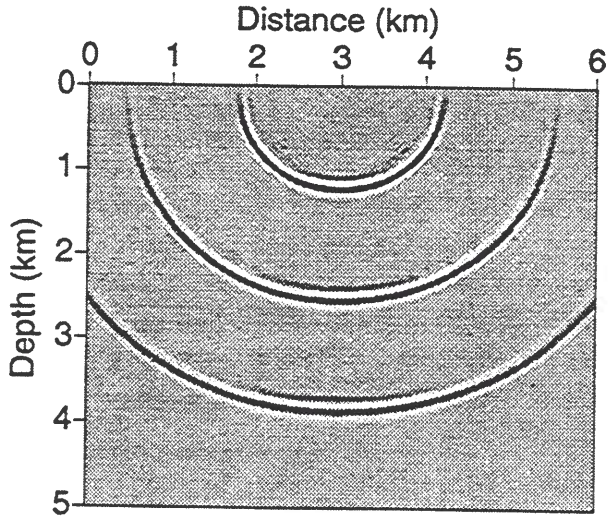

FIG. 6.15. Migration impulse responses by the leapfrog finite-difference method with the full FCT correction ($\eta_1 = 0.05$; $\eta_2 = 0.062$).

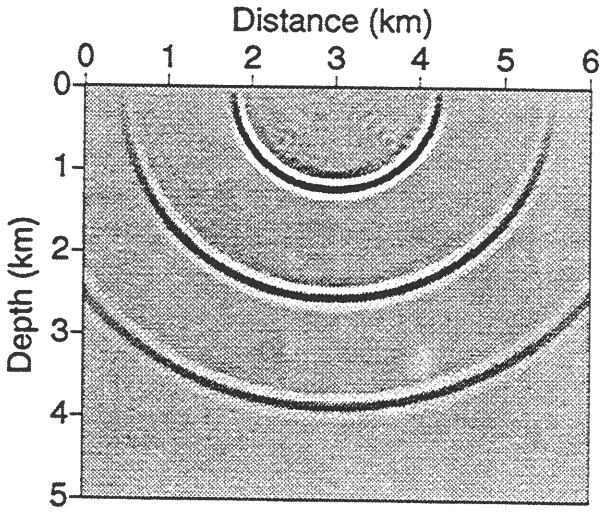

FIG. 6.17. Migration impulse responses by the leapfrog finite-difference method with the optimized FCT approach ($\eta = 0.1$).

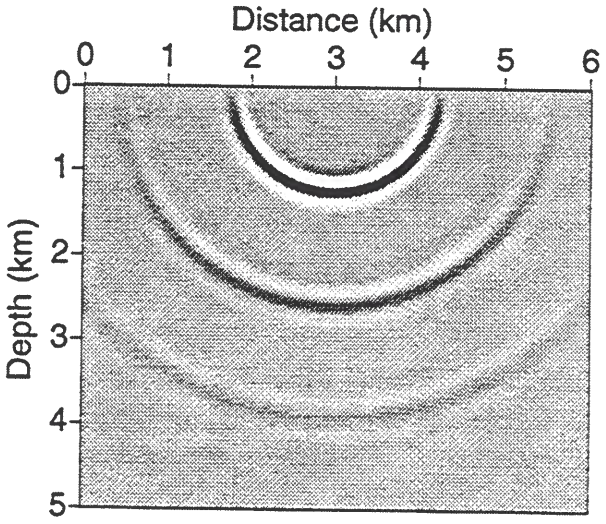

FIG. 6.18. Migration impulse responses by the pseudo Lax-Wendroff finite-difference method without the FCT correction.

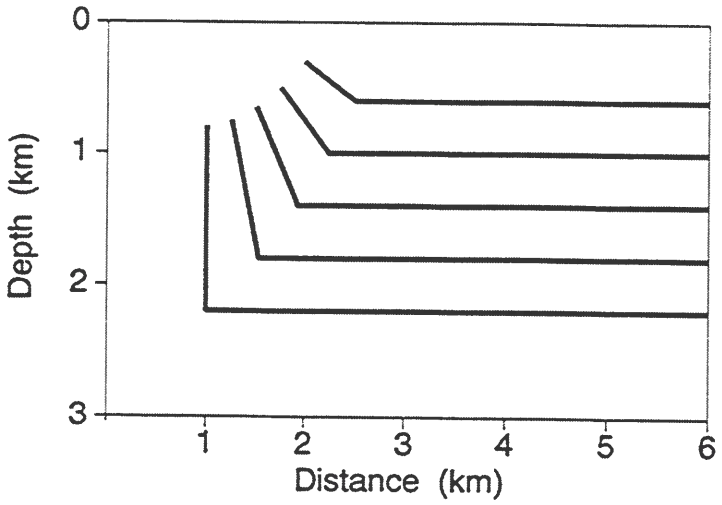

FIG. 6.20. Reflector model used to generate synthetic data for the tests described in Figures 6.22 through 6.24.

(Figure 6.21b). Due to the lateral variation in velocity, wavelets for the horizontal events broaden to the right.

6.2 Second-order system

This section again shows FCT-corrected modeling and migration results, but this time based on the second-order acoustic wave equation (2.1).

6.2.1 Modeling for a wedge model

Figure 6.25 shows a two-dimensional model in which the velocity in a rectangular area is set at zero, while outside that area the velocity is a constant 2.438 km/s. The modeled area in the tests is 5.266×5.266 km^2 with the upper left corner of the rectangular region at (2.194 km, 3.510 km) and a line source located at (2.633 km, 3.072 km). The time variation of the source function is $-(t-0.1)e^{-\alpha(t-0.1)^2}$, where $t \geq 0$ is time, measured in s, and α=700 s^{-2}. This source function has an upper half-power frequency of 10 Hz, and the corresponding half-power wavelength is about 0.244 km for velocity v=2.438 km/s. Here, three different grid sizes, fine (Δx=0.02194 km; $G_0 \approx 11$), medium (Δx=0.04388 km; $G_0 \approx 5.5$) and coarse (Δx=0.08776 km; $G_0 \approx 2.7$), have been tested.

Figure 6.26a shows the snapshot at 1.026 s for the wavefield computed by the second-order (in space and time) conventional finite-difference method over the fine grid, and Figure 6.26b shows the snapshot at the same time for the FCT-corrected wavefield. For this fine sampling, both the conventional finite-difference result and the FCT-corrected result are accurate and show no numerical dispersion.

On the medium grid, for which $G_0 \approx 5.5$, the wavefield obtained by the conventional finite-difference approach becomes dispersive (Figure 6.26c). The FCT correction, how-

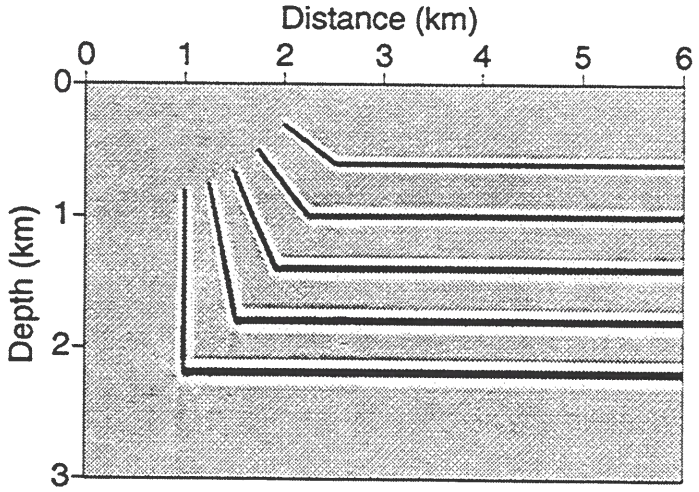

FIG. 6.23. Migrated section for velocity model $c(z) = 1.6 + 0.6z$ km/s, and constant density by the leapfrog scheme with the full FCT correction.

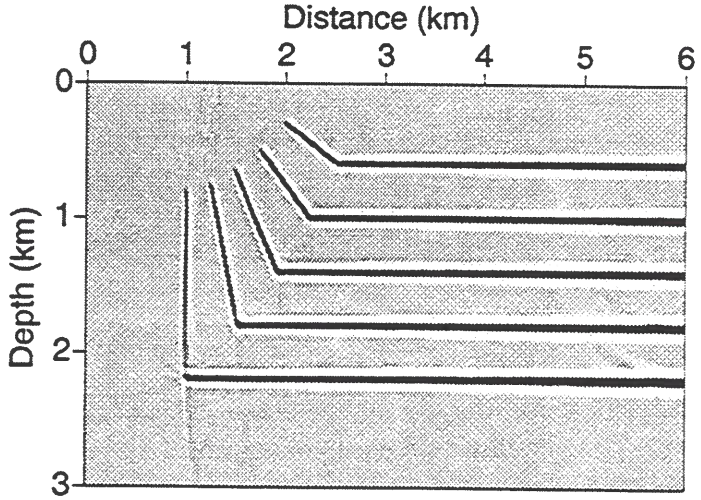

FIG. 6.24. Migrated section for velocity model $c(x, z) = 1.5 + 0.2x + 0.35z$ km/s, and constant density by the leapfrog scheme with the full FCT correction.

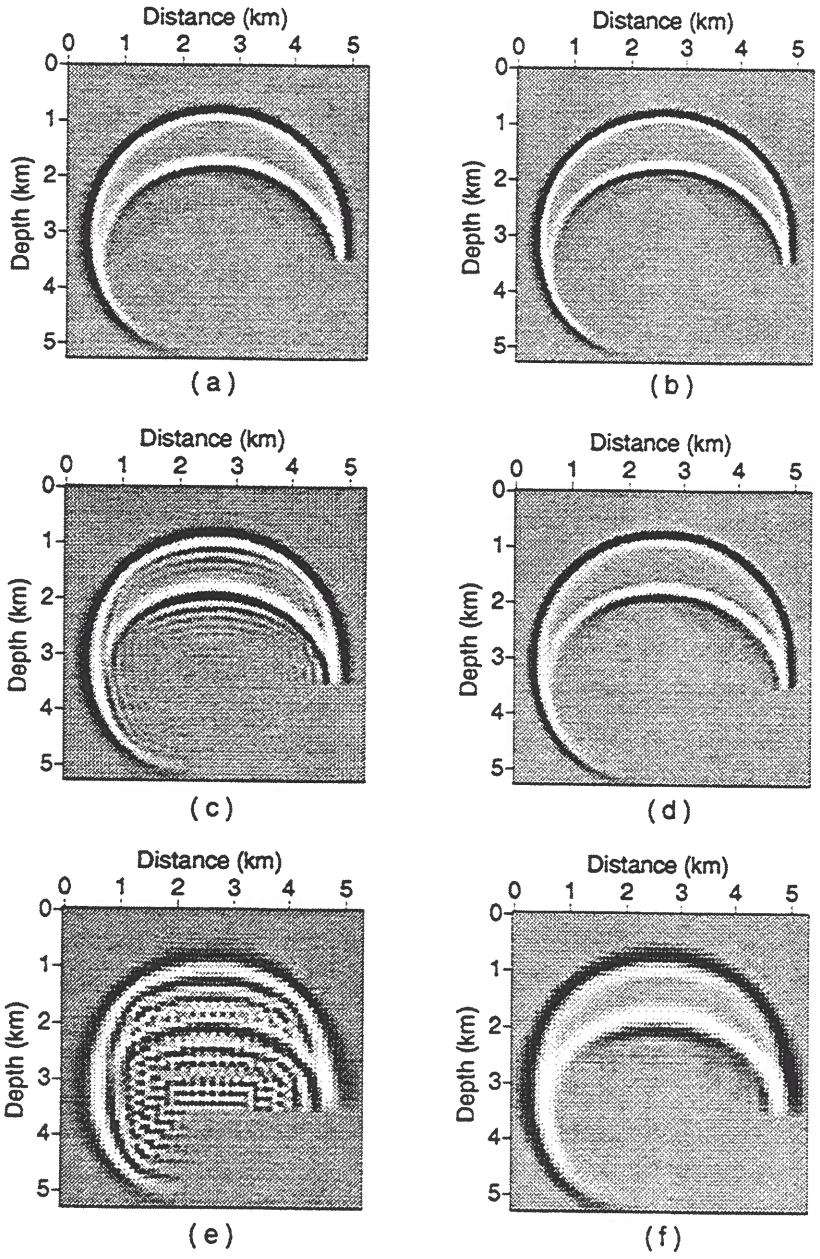

FIG. 6.26. Wavefield snapshots for different grid coarseness. (a) and (b) are for a fine grid ($G_0 \approx 11$); (c) and (d) are for a medium-coarseness grid ($G_0 \approx 5.5$); and (e) and (f) are for a coarse grid ($G_0 \approx 2.7$). (a), (c) and (e) are solutions by the conventional finite-difference method, and (b), (d) and (f) are solution with the full FCT correction.

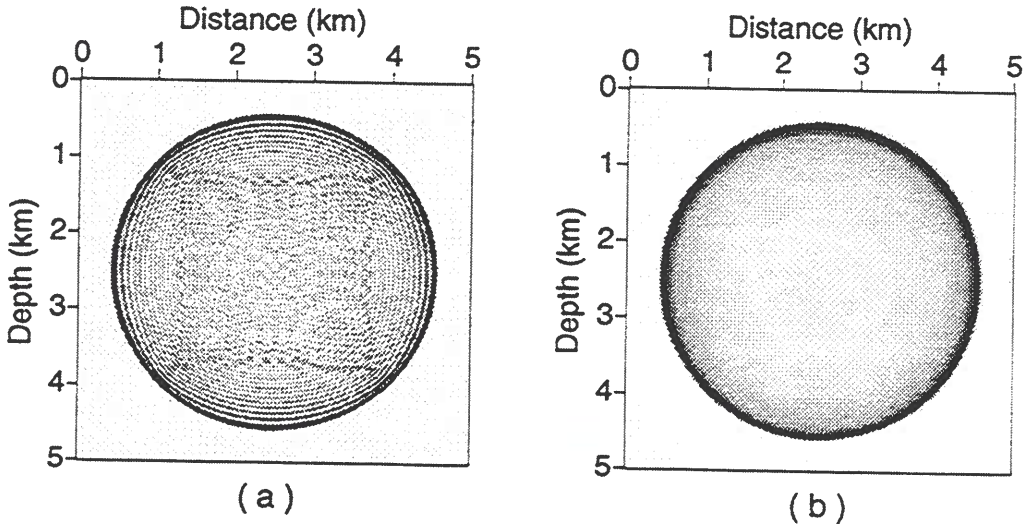

FIG. 6.27. Snapshot of a two-dimensional wavefield for an impulse in both time and space. (a) Solution by the fourth-order conventional finite-difference method. (b) Solution with the FCT correction.

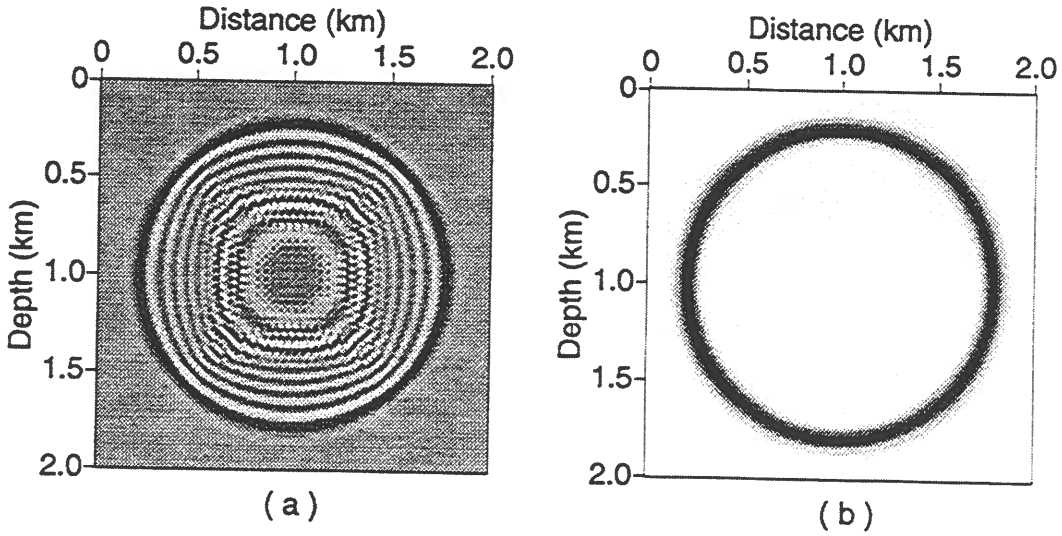

FIG. 6.28. Cross section of a three-dimensional wavefield snapshot for an impulse in both time and space. (a) Solution by the fourth-order conventional finite-difference method. (b) Solution with the FCT correction.

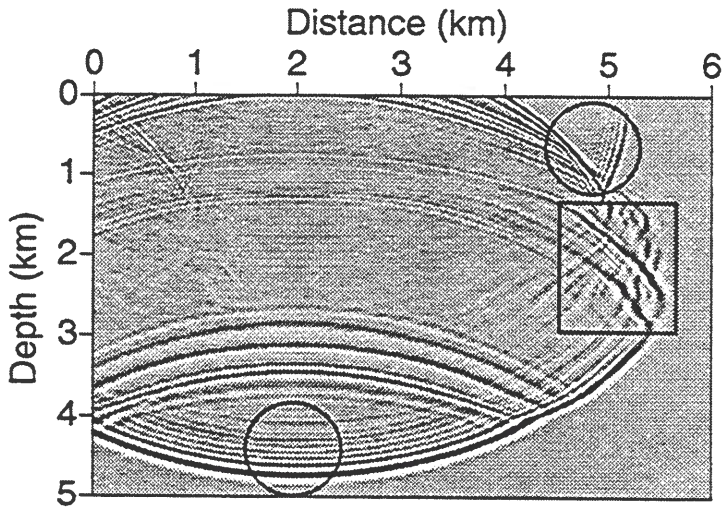

FIG. 6.30. Wavefield snapshot at $t = 2.175$ s in the thin-layered model shown in Figure 6.30, generated by the fourth-order finite-difference method ($G_0 \approx 4.4$ at z=0 km).

numerical dispersion, while at the same time it restores much of the (lower-frequency) true wave, including multiple reflections, at each time step.

When applying the optimized FCT correction to the conventional finite-difference solution, we obtain the same desirable result, the elimination of numerical dispersion and preservation of the true wavefield oscillations, as seen in Figure 6.32. In Chapter 8, the relative costs of the full FCT correction and optimized FCT correction in the entire finite-difference method are discussed.

6.2.4 Modeling in media with a localized low-velocity zone

Figure 6.33 shows a model consisting of two homogeneous layers. In the first layer (from surface to 1.5 km depth), the velocity is 1.8 km/s, while in the second layer (below 1.5 km depth), the medium has a relatively high velocity of 3.6 km/s. The spatial step used in the modeling tests is 0.02 km in both horizontal and vertical directions. The line source, a 15-Hz Ricker wavelet, is located at (3 km, 1.5 km). The corresponding number of grid points per upper half-power wavelength is about 3.7 in the low-velocity layer and 7.4 in the high-velocity layer.

For this grid size, the fourth-order conventional finite-difference method can generate numerical dispersion in the low-velocity layer; however, in the high-velocity layer there is no numerical dispersion, as seen in Figure 6.34. With the full FCT correction applied to the entire modeled area, the solution shows no numerical dispersion (Figure 6.35). However, since the numerical dispersion is generated in just the low-velocity layer, we can gain savings in computational effort by restricting the FCT correction to just that

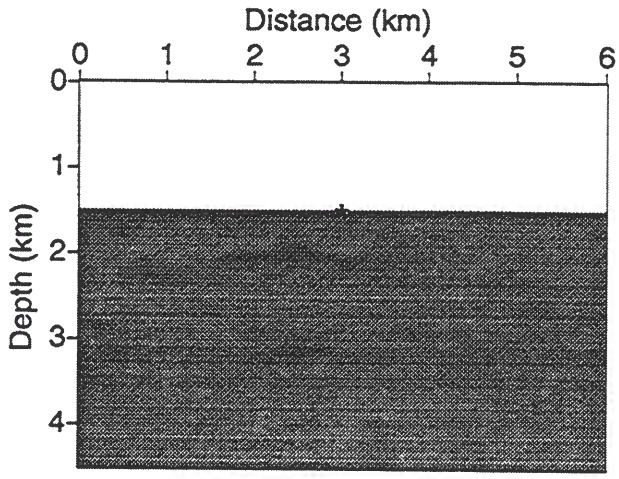

FIG. 6.33. Velocity model used to generate wavefield snapshots given in Figures 6.34 through 6.36. Darker shading indicates high velocity, and the asterisk denotes the source location.

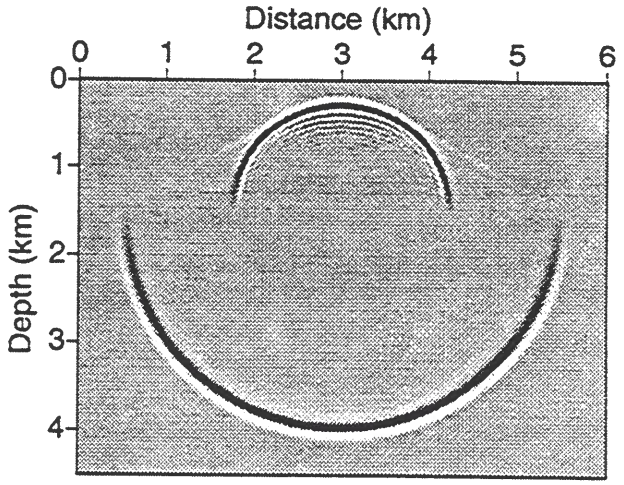

FIG. 6.34. Wavefield snapshot at $t = 0.75$ s in the two-layered model shown in Figure 6.33, generated by the fourth-order finite-difference method without the FCT correction.

layer. In this manner, only one-third as much effort is required for the FCT correction, yet the solution shows no indication of numerical dispersion (as seen in Figure 6.36). The optimized FCT can similarly be applied to only the low-velocity zone, reducing the computation effort of the FCT correction further. That solution (not shown here) shows no numerical dispersion as well.

The savings in the FCT computation depends on the relative size of the low velocity zone. Clearly, for homogeneous media, for example, the FCT correction gains no such benefit; the FCT correction needs to be applied throughout the modeled area.

6.2.5 Migration of data from a salt-dome structure model

Figure 6.37 shows a reflector structure modeling the boundary of an overhanging salt dome, with dip as large as 125 degrees. The input zero-offset time section for velocity linearly increasing with depth [$c(z) = 1.5 + 0.9z$ km/s] was obtained by a Kirchhoff modeling program. The wavelet used in the modeling was a symmetric Ricker wavelet with dominant frequency of 30 Hz. Figures 6.38 through 6.42 show the reverse-time depth-migration results by the second-order and the fourth-order conventional finite-difference methods, without and with the FCT correction.

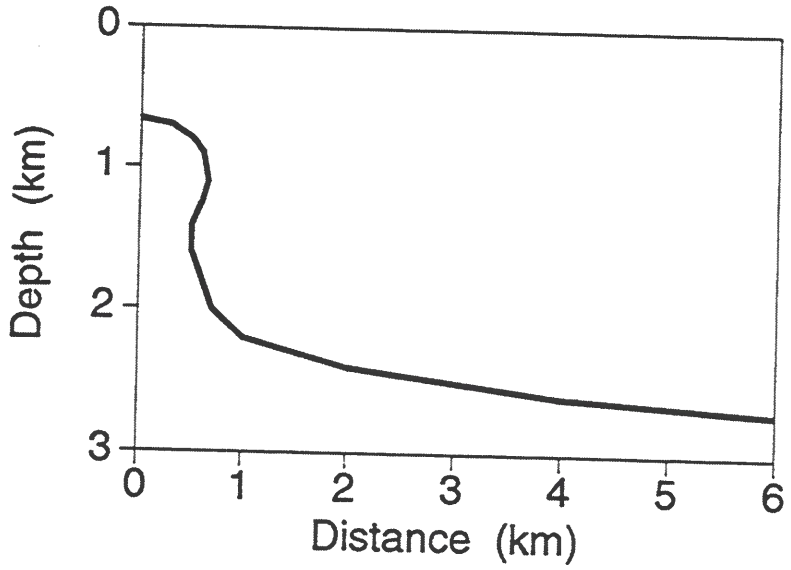

FIG. 6.37. Reflector model used to generate synthetic data for the tests described in Figures 6.38 through 6.42.

For Figure 6.38 (a migration image by second-order conventional finite-difference method), the number of grid points per upper half-power wavelength at depth z=0 km, where velocity is lowest (1.5 km/s), is about 3.7 (very coarse grid). Since the grid remains

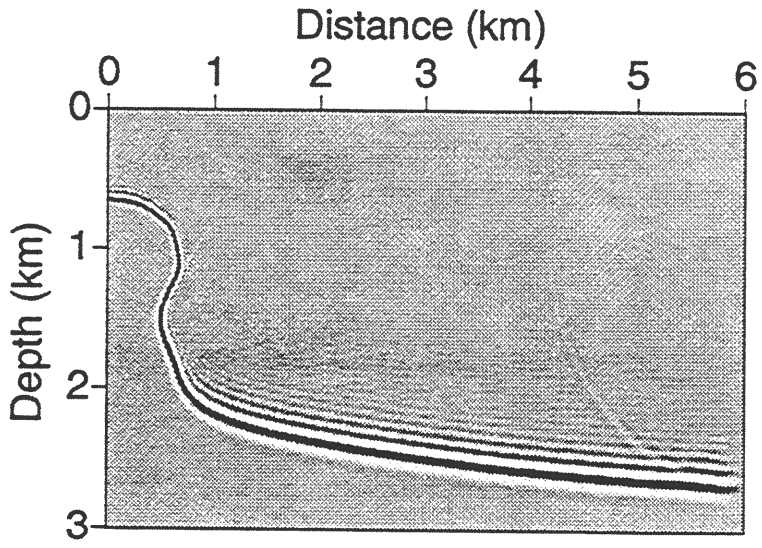

FIG. 6.39. Fourth-order conventional finite-difference migration for the same grid as that for Figure 6.38.

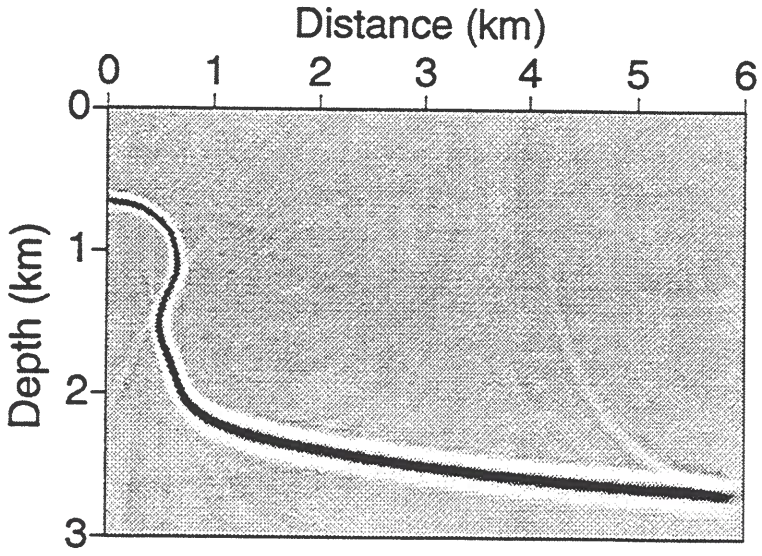

FIG. 6.40. Second-order finite-difference migration with the full FCT correction for the same grid as that for Figure 6.38.

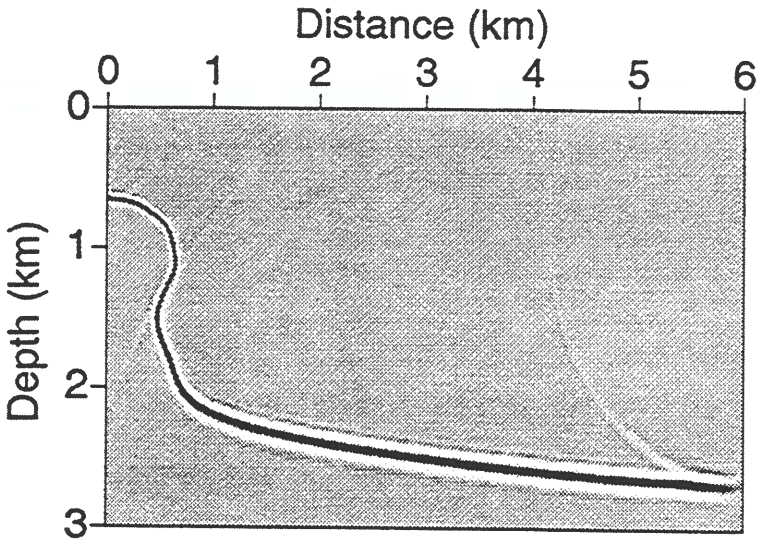

FIG. 6.43. Fourth-order finite-difference migration with the optimized FCT correction for the same grid size as that for Figure 6.38.

yields the desired resolution (compare with Figures 6.38 through 6.40), plus the computational savings over the fourth-order method on the medium grid. The optimized FCT correction applied to the fourth-order method on the coarse grid (Figure 6.43) also yields the desired solution.

6.2.6 Migration of field data

Figure 6.44 shows a stacked section, after application of dip-moveout (DMO) correction, from the Gulf of Mexico. For these data, the dominant frequency at 2 s is about 35 Hz, and the background velocity varies from 1.5 to 3.3 km/s. The spatial step size in both horizontal and vertical directions is 6 m, so the lowest number of sample points per upper half-power wavelength here is about 3.7. To satisfy the stability condition for this 2-D problem [the stability condition for 1-D problems, equation (3.72), is changed to $\Delta t \leq \frac{\Delta x}{\sqrt{2}c}$ for the 2-D problem], the time step is 1.1 ms. The migrated section by the fourth-order conventional finite-difference method is shown in Figure 6.45, and the part of the image inside the dashed box is enlarged in Figure 6.46. For comparison, Figure 6.47 shows a closeup view of a comparable portion of the unmigrated DMO-stacked section. The arrows in Figures 6.46 and 6.47 point to equivalent positions on the two sections, where reflections have little slope and therefore should not be changed much by the migration. One might suspect, then, that the added reflection events at the arrow in Figure 6.46 are artifacts of numerical dispersion. With the FCT correction (Figure 6.48), the suspect events are removed. Applying the less costly, optimized FCT correction yields a result (Figure 6.49) with the added events removed as well.

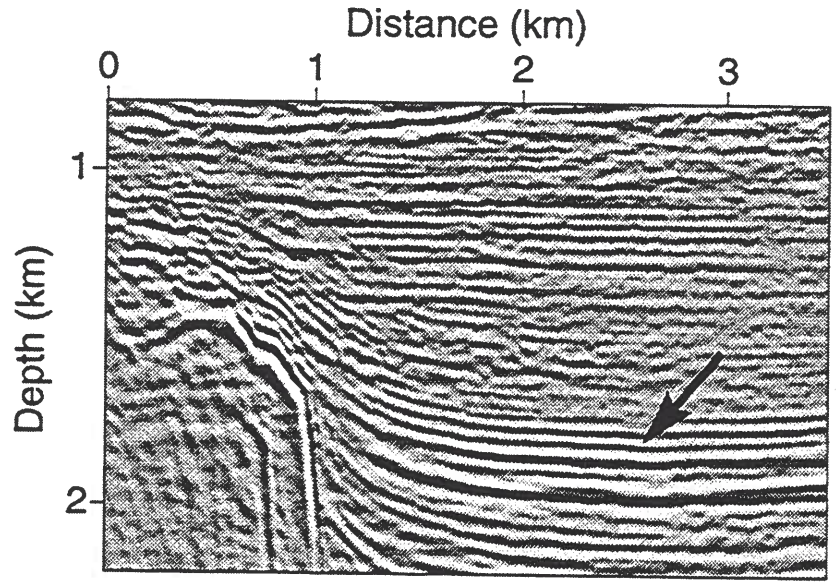

FIG. 6.46. Enlarged portion of migration result by the fourth-order conventional finite-difference method.

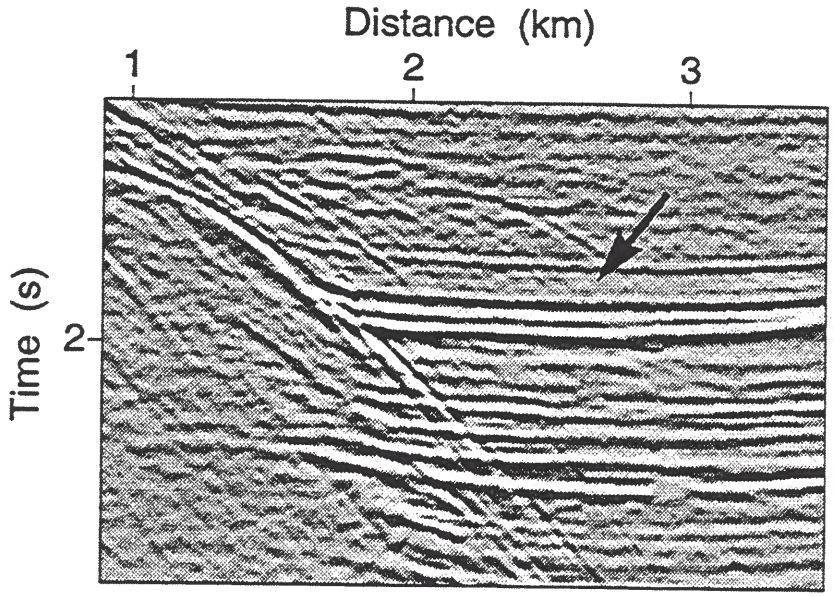

FIG. 6.47. Detail of DMO and stacked section from Gulf of Mexico.

Chapter 7

APPLICATION TO ELASTIC MEDIA

In this chapter, I show examples of the FCT algorithm in two-dimensional forward modeling for homogeneous and inhomogeneous elastic isotropic media, transversely isotropic media, and a layered TI medium. For each medium, P- and SV-waves, as well as SH-waves, are computed. In each of the tests, the spatial steps Δx and Δz are 0.02 km, and the time step Δt is chosen to satisfy the stability condition, $\Delta t \leq \Delta x/\sqrt{\alpha^2+\beta^2}$ (Kelly et al., 1976; α is the P-wave velocity and β is the S-wave velocity). I also present examples of three-dimensional forward modeling and two-dimensional reverse-time migration for TI media.

Test results show that, for elastic media, as for acoustic media, the FCT method on a coarse grid produces accurate wavefield snapshots and migration images without numerical dispersion.

7.1 Snapshots in two-dimensional isotropic media

Figures 7.1 through 7.3 show snapshots at 0.64 s for two elastic isotropic media with constant density. The line source, with a 20-Hz Ricker wavelet assigned to force components f_1, f_2 and f_3, is located at (2.5 km, 2.5 km). Force components f_1 and f_3 generate the P- and SV-waves, while the force component f_2 generates the SH-wave. The directions of the force are indicated in Figures 7.1 and 7.2 .

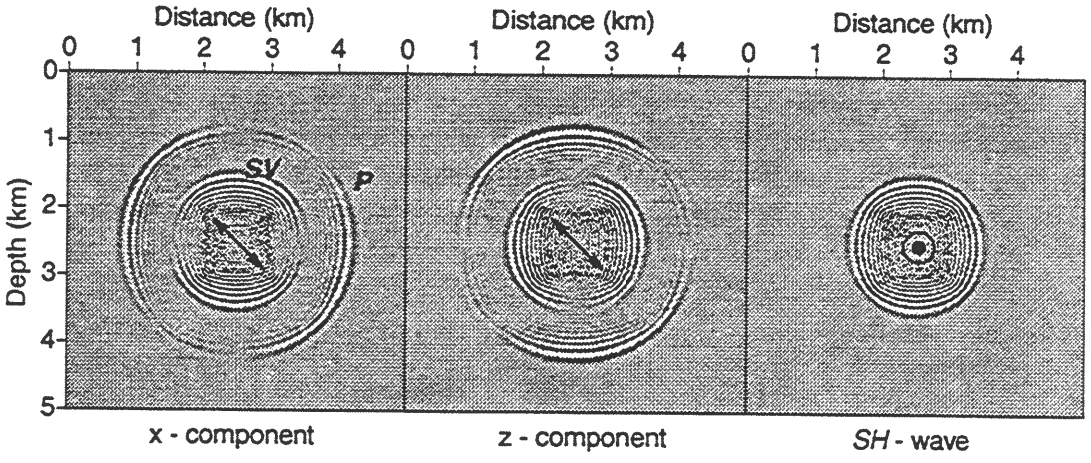

FIG. 7.1. Snapshots for a homogeneous elastic, isotropic medium with a P-wave velocity of 3.0 km/s and an S-wave velocity of 1.8 km/s.

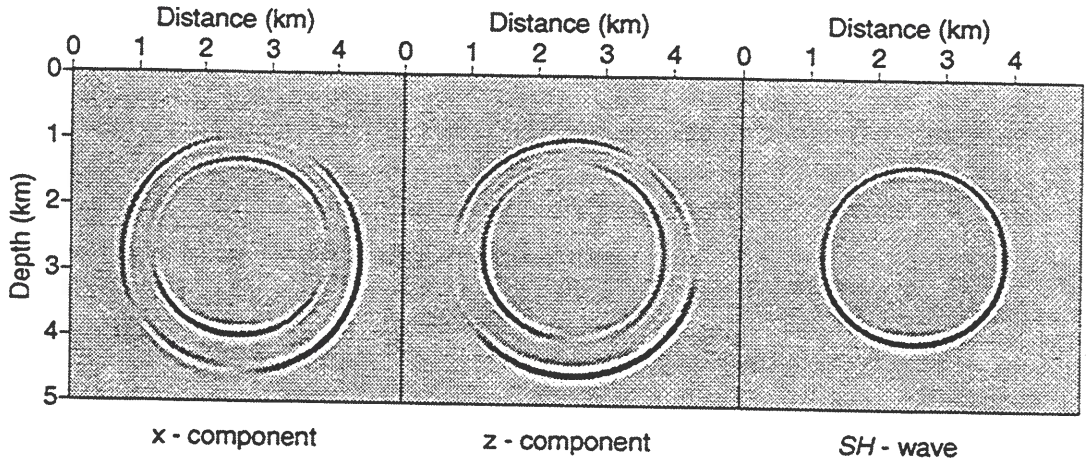

FIG. 7.3. Snapshots for an elastic isotropic medium with linear velocity variation. P-wave velocity is $\alpha = 1.5 + 0.1x + 0.5z$ km/s, and S-wave velocity is $\beta = 1.0 + 0.1x + 0.4z$.

Material	α_0 (km/s)	β_0 (km/s)	ε	δ	γ	ρ (g/cm^3)
Sandstone-shale	3.009	1.654	0.013	-0.001	0.0035	2.34
Mesaverde-shale	3.749	2.621	0.128	0.078	0.1	2.92
Cotton Valley shale	4.721	2.89	0.135	0.205	0.18	2.64
Limestone-shale	3.306	1.819	0.134	0.0	0.156	2.44
Taylor sandstone	3.368	1.829	0.11	-0.035	0.255	2.5
Anisotropic-shale	2.745	1.508	0.103	-0.001	0.345	2.34
Anisotropic*	2.0	0.894	0.0	-0.241	0.4	2.4
Mesaverde clayshale	3.928	2.055	0.334	0.73	0.575	2.59
Gypsum-weathered material	1.911	0.795	1.161	-0.14	2.781	2.35

Table 7.1. Thomsen parameters for several materials (Thomsen, 1986). *Medium with Thomsen parameters designed here to test wavefront behavior for ε=0 and relatively large δ and γ.

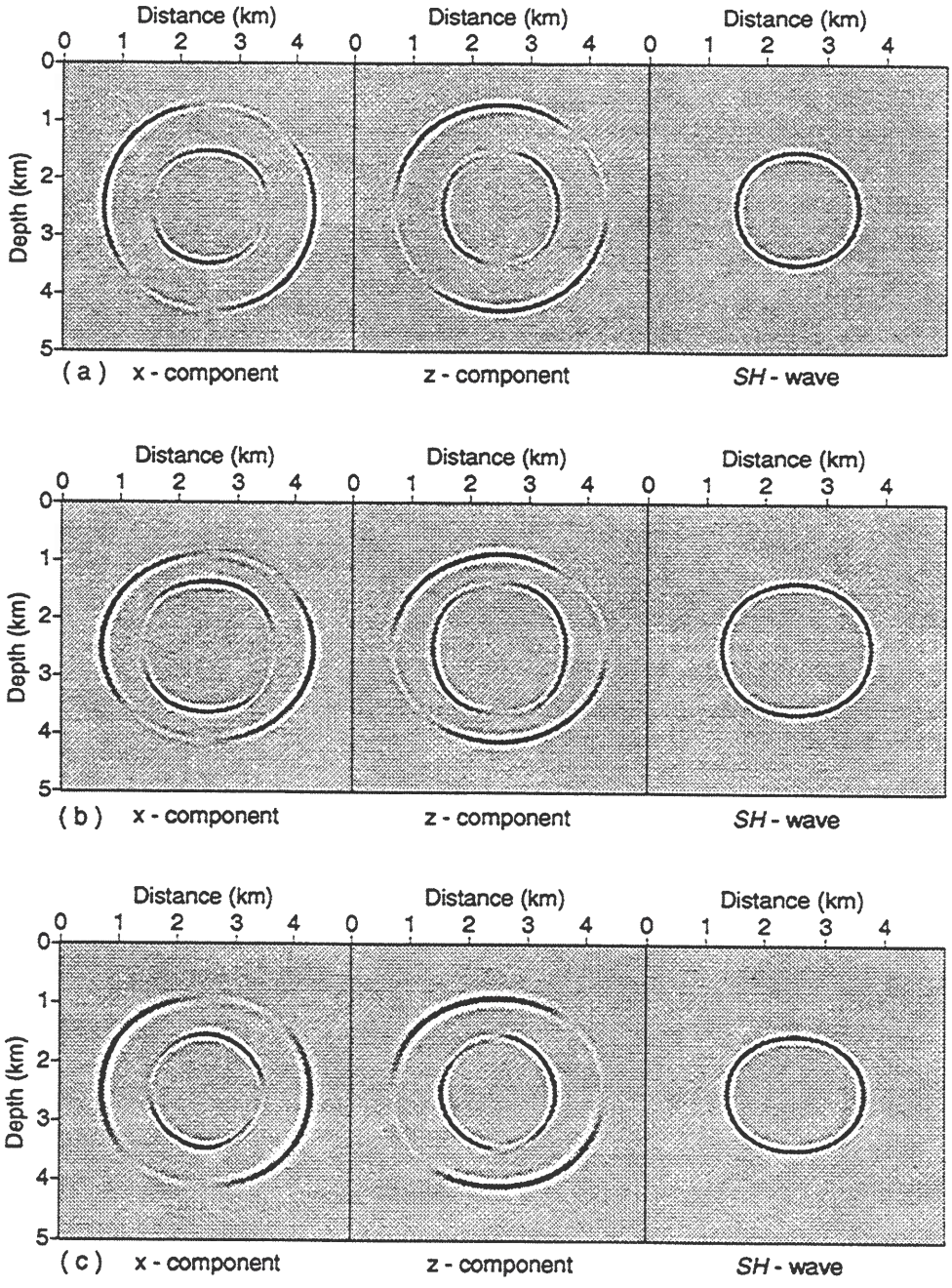

FIG. 7.4. Wavefield snapshots for "mildly" anisotropic media: (a) sandstone-shale; (b) Mesaverde shale; and (c) Cotton Valley shale.

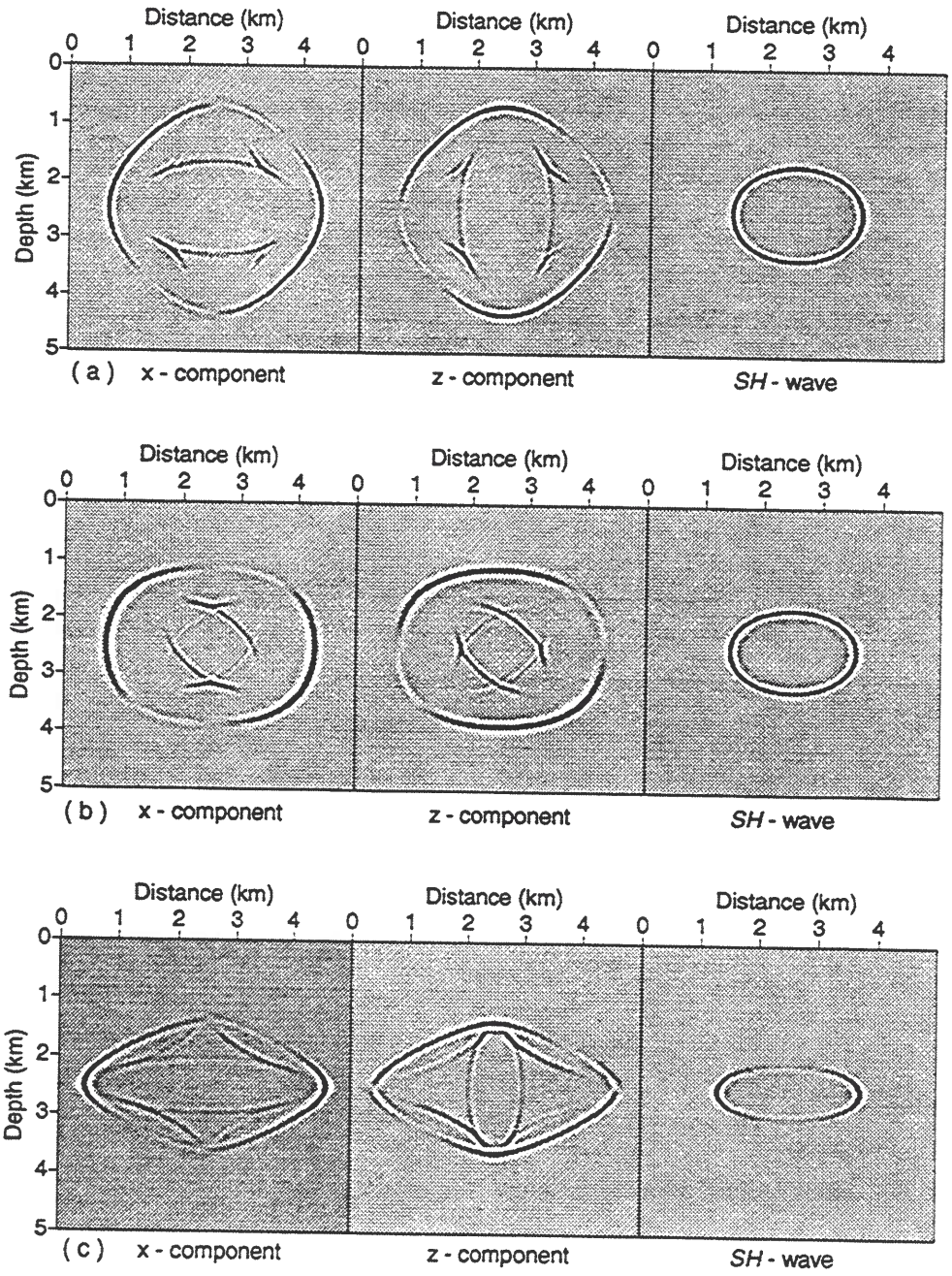

FIG. 7.6. Wavefield snapshots for media that are considered strongly anisotropic. (a) medium with α_0=2.0 km/s, β_0=0.894 km/s, ε=0.0, γ=0.4, δ=-0.241 and ρ=2.4 g/cm^3; (b) Mesaverde clayshale; and (c) gypsum-weathered shale.

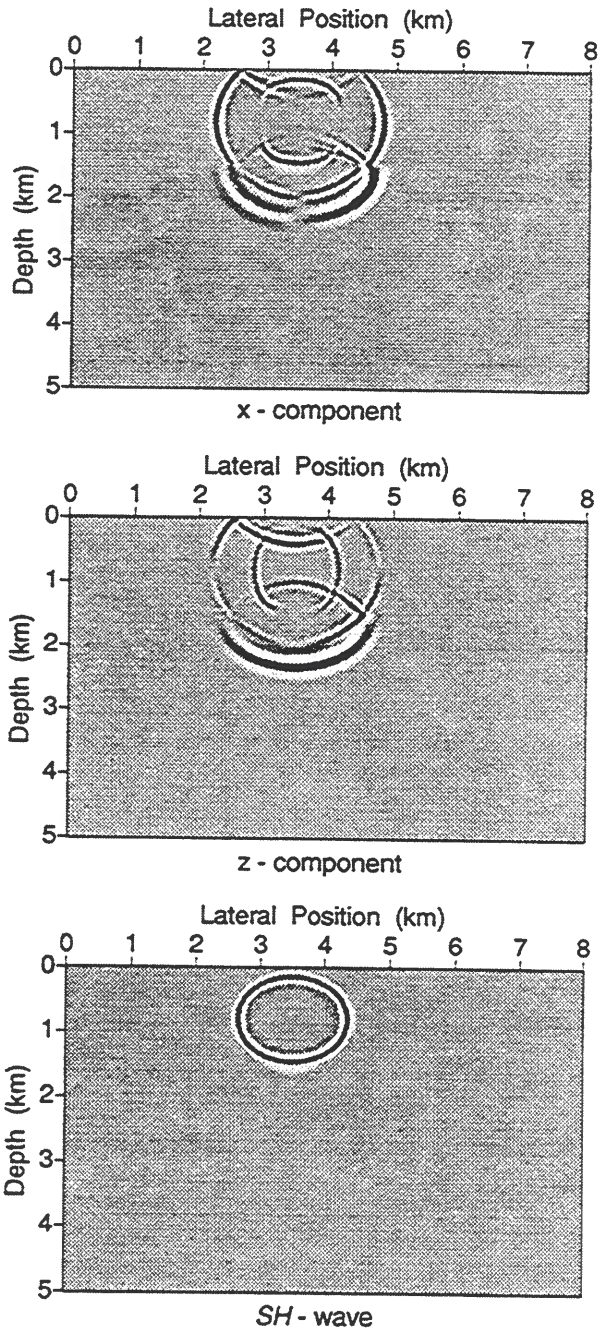

FIG. 7.8. Snapshots of x-, y-, and z-components at 0.48 s for the layered medium in Figure 7.7.

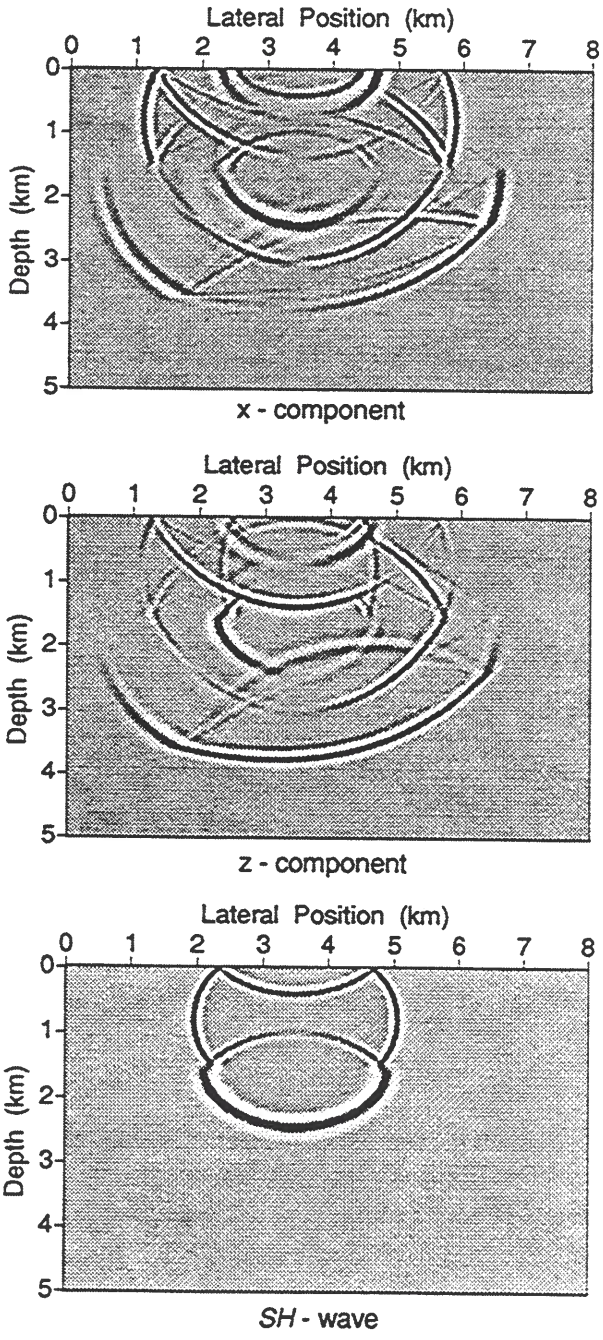

FIG. 7.10. Snapshots of x-, y-, and z-components at 0.84 s for the layered medium in Figure 7.7.

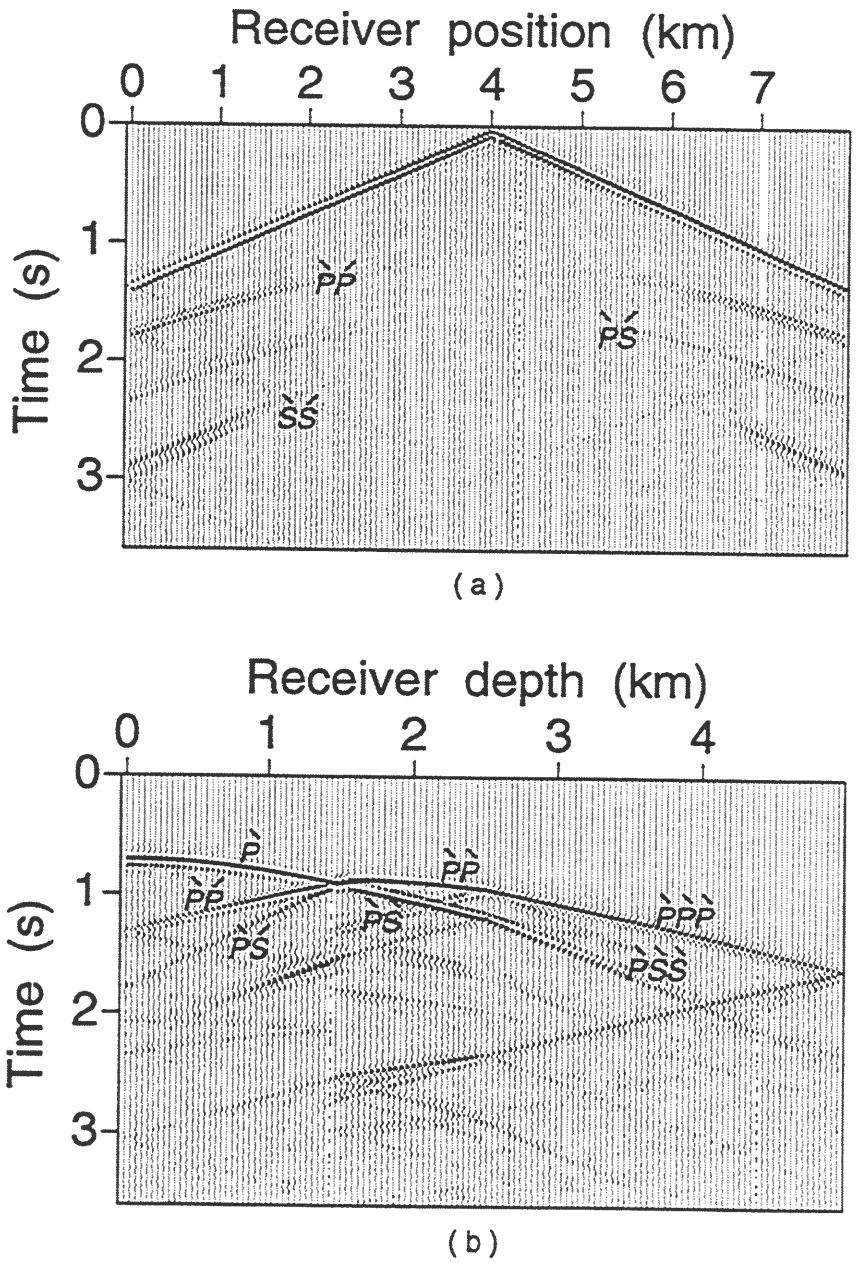

FIG. 7.12. In-line horizontal-motion seismograms for a vertical displacement source in the layered model of Figure 7.11. (a) Surface seismic reflection seismogram. (b) VSP seismogram.

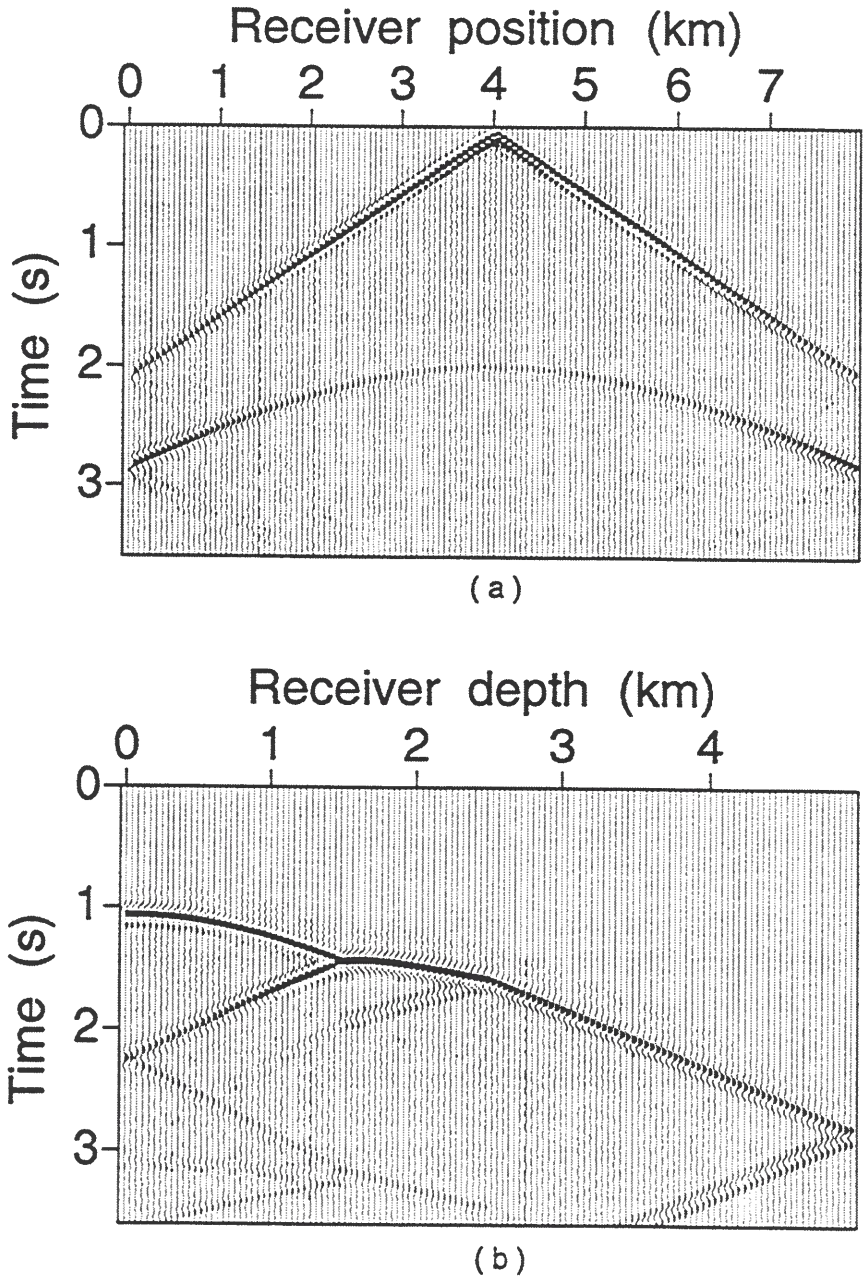

FIG. 7.14. *SH*-wave seismograms for the layered model of Figure 7.11. (a) Surface seismic reflection seismogram. (b) VSP seismogram.

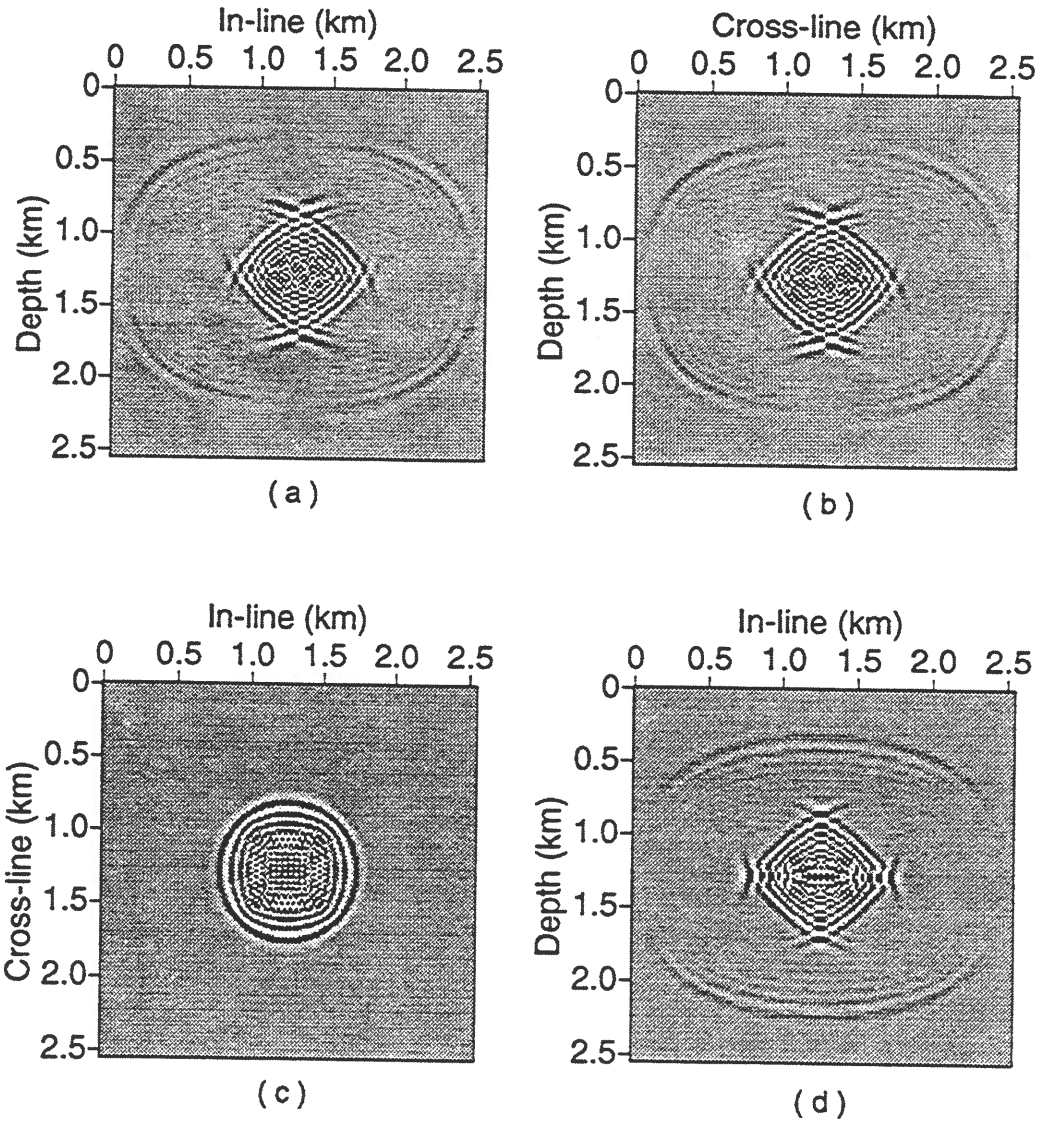

FIG. 7.15. Wavefield snapshots, at time t=0.27 s, in Mesaverde clayshale, generated by the fourth-order conventional finite-differencing. (a) x-component in the xz-plane (i.e. in-line vertical plane), (b) y-component in the yz-plane (i.e. cross-line vertical plane), (c) z-component in the xy-plane (i.e. horizontal plane), and (d) z-component in the xz-plane (i.e. in-line vertical plane).

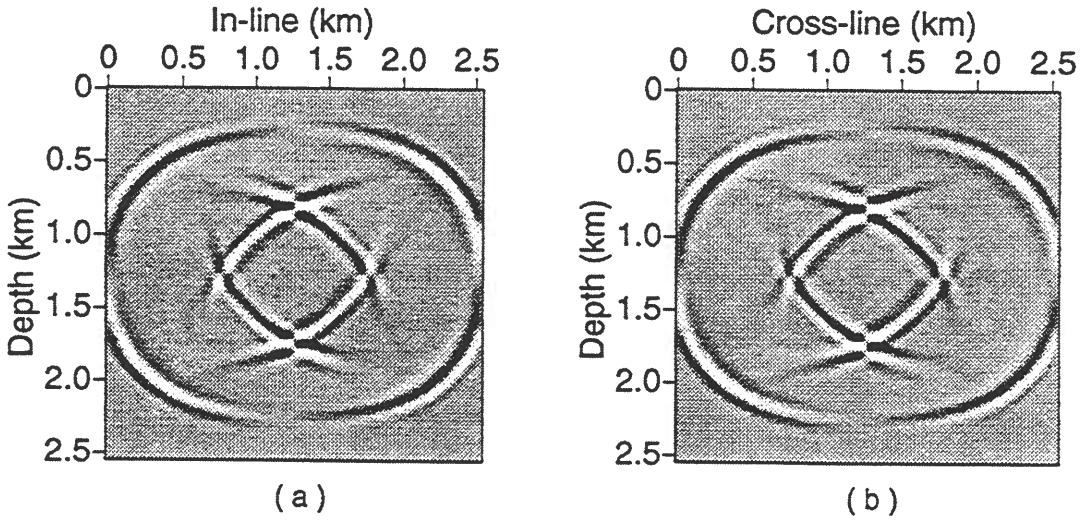

FIG. 7.17. Wavefield snapshots, at time t=0.27 s, in Mesaverde clayshale, generated by fourth-order finite-differencing with the FCT correction. (a) x-component in the xz-plane (i.e. in-line vertical plane), and (b) y-component in the yz-plane (i.e. cross-line vertical plane).

7.6 Migration in two-dimensional TI media

Figure 7.19 shows a depth section modeling a fault structure with two horizontal segments and one 45-degree dipping segment. Zero-offset time sections were generated for the TI shale of Jones and Wang (1981) ($\alpha_0 = 3.048$ km/s, $\beta_0 = 1.490$ km/s, δ = -0.05, $\epsilon = 0.255$ and $\gamma = 0.48$) by using the finite-difference method with the FCT correction. To obtain the zero-offset time sections, I place the sources on the reflectors and record the wavefield at the surface. Figures 7.20a and 7.20b give the x- and z-component of the data with vertical sources, while Figure 7.20c gives the SH-wave component with the source in the y-direction. The time variation of the source function is a symmetric Ricker wavelet with a dominant frequency of 15 Hz, and the number of grid points per upper half-power wavelength is coarse ($G_p \approx 6.2$) for the P-waves, and coarser ($G_s \approx 3$) for the S-waves along the symmetry-axis direction.

In Figure 7.20a, showing the x-component of the displacement (i.e., in-line component), P- and SV-waves from only the dipping reflector have been recorded, while, due to the symmetry for the vertical source, the signal from the horizontal reflector has no component in the in-line horizontal direction. In contrast, the z-component (vertical), shows signals from both the horizontal and dipping reflectors. Since the SH-wave is decoupled from the P- and SV-waves, Figure 7.20c gives only the SH-wave.

Migrated images from the synthetic data (Figure 7.20) are shown in Figures 7.21 and 7.22. In Figure 7.21a, which shows the image from the x-component, the horizontal

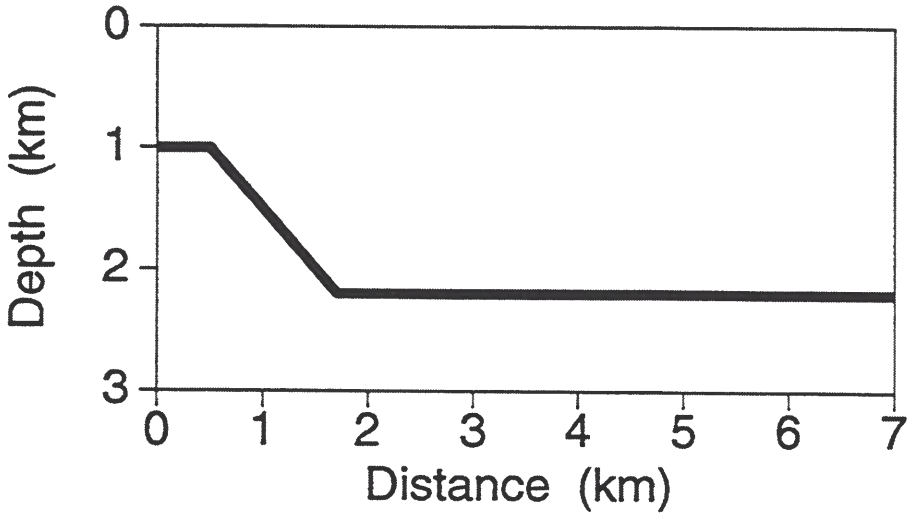

FIG. 7.19. Dip-direction (x-z plane) section showing a reflector model used to generate the synthetic data in Figures 7.20 for the tests described in Figures 7.21 and 7.22.

portions of the reflector cannot be imaged because those portions produced no information in the x-component. The dipping reflector, however, is well imaged. Figure 7.21b gives the image from the z-component, which shows both the horizontal and dipping reflectors in the correct position. The dipping reflector, however, appears weak since the corresponding image is generated from both P- and SV-components, and minor phase error can introduce significant amplitude error. The image shown here is obtained by migrating the full data set (both horizontal and vertical components), which contains both the P- and SV-wave components. Perhaps a better approach would have been to separate the P- and S-waves before migration.

The migration image based on the SH-wave data is shown in Figure 7.22. Again, the imaged reflector is correctly positioned and well imaged.

7.7 Modeling in two-dimensional TI media with a tilted axis of symmetry

Figures 7.23 and 7.24 each shows a set of nine wavefield snapshots (at time t =0.45 s) in a homogeneous Mesaverde clayshale (Thomsen, 1986; α_0 =3.928 km/s, β_0 =2.055 km/s, $\epsilon = 0.334$, $\delta = 0.73$, $\gamma = 0.575$) with various orientations of the symmetry axis for this TI medium. The variable that determines the orientation of the symmetry axis is θ (the angle between the vertical direction and the symmetry axis direction). In Figure 7.23b, the double sided dashed arrow in the SH-wave component indicates an example

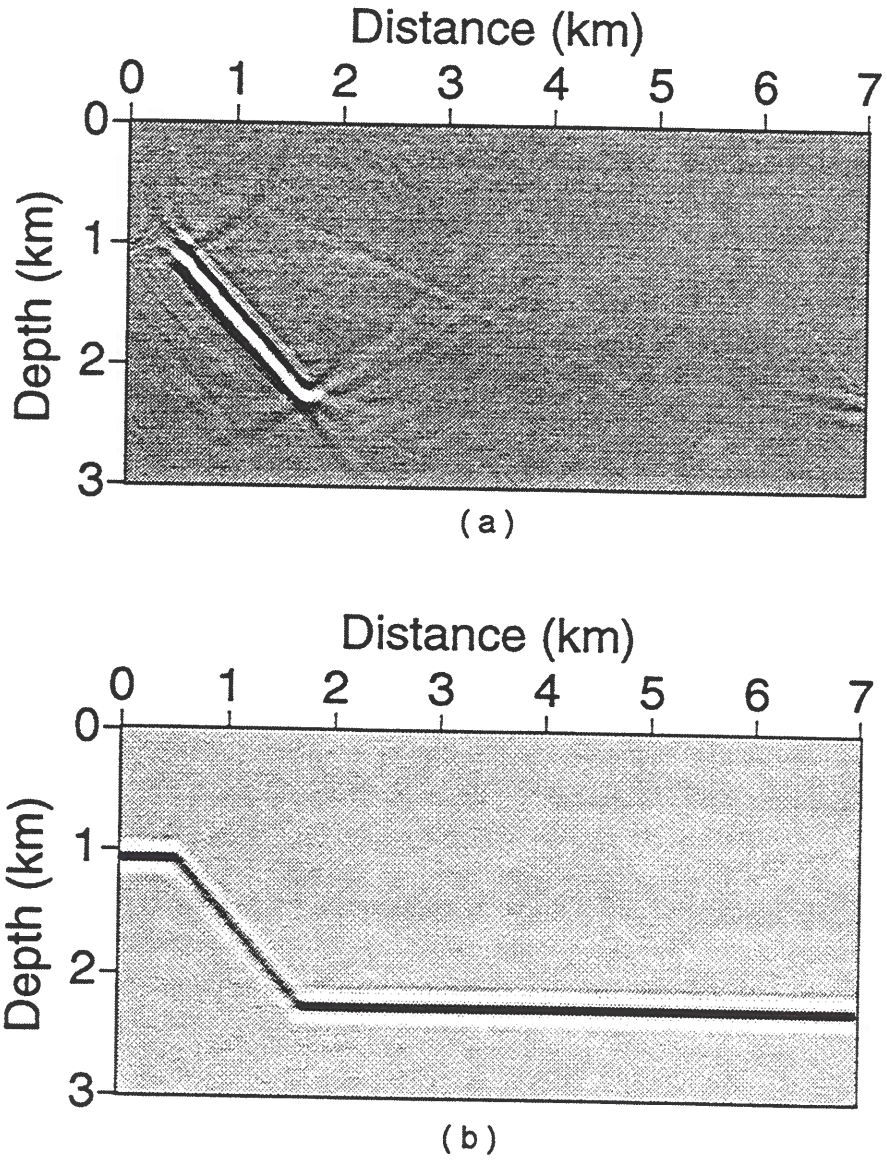

FIG. 7.21. Migrated section for shale of Jones and Wang (1981) from both P- and SV-wave. (a) image from the x-component, and (b) image from the z-component.

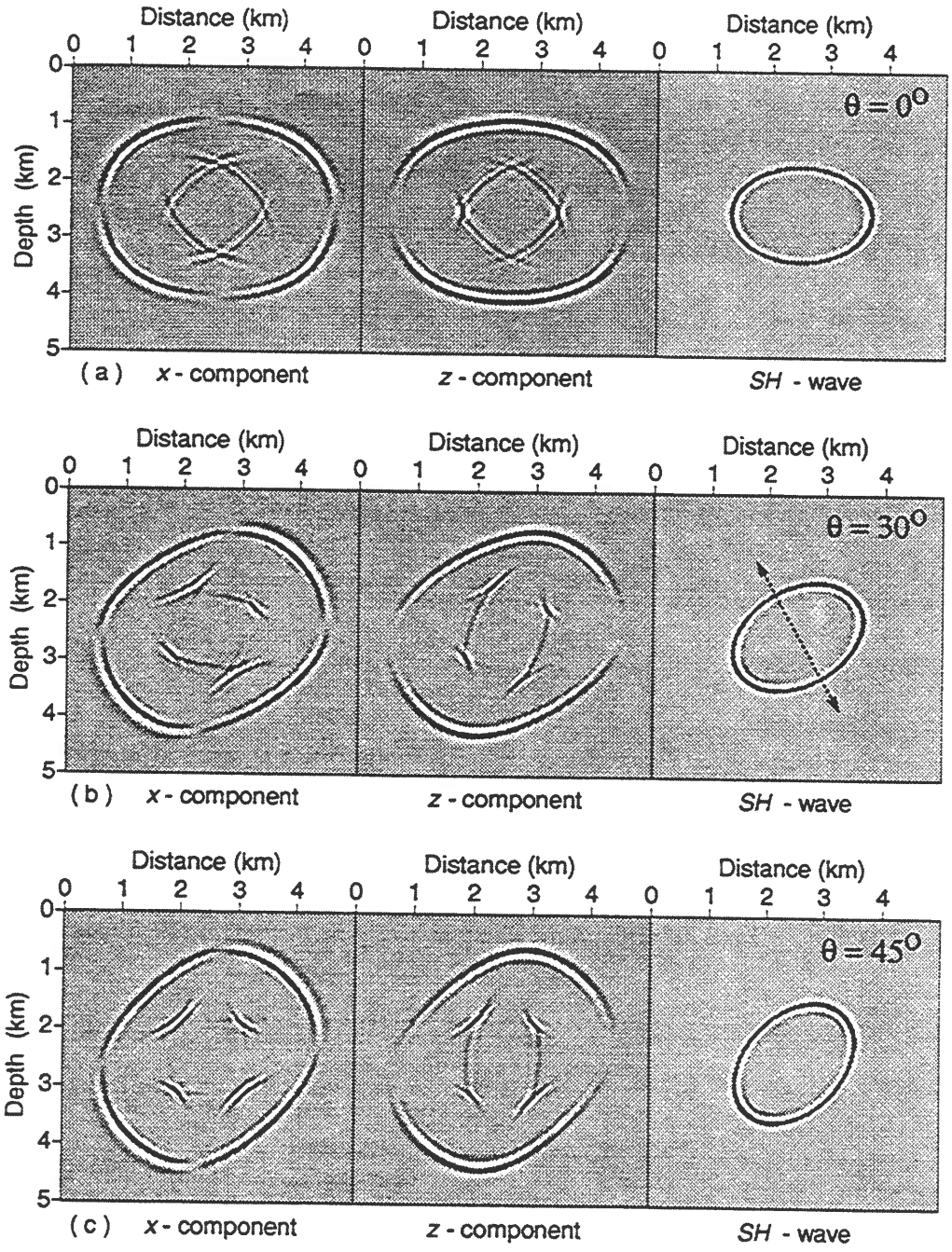

FIG. 7.23. Wavefield snapshots in Mesaverde clayshale with a tilted axis of symmetry. (a) $\theta = 0°$, (b) $\theta = 30°$, and (c) $\theta = 45°$.

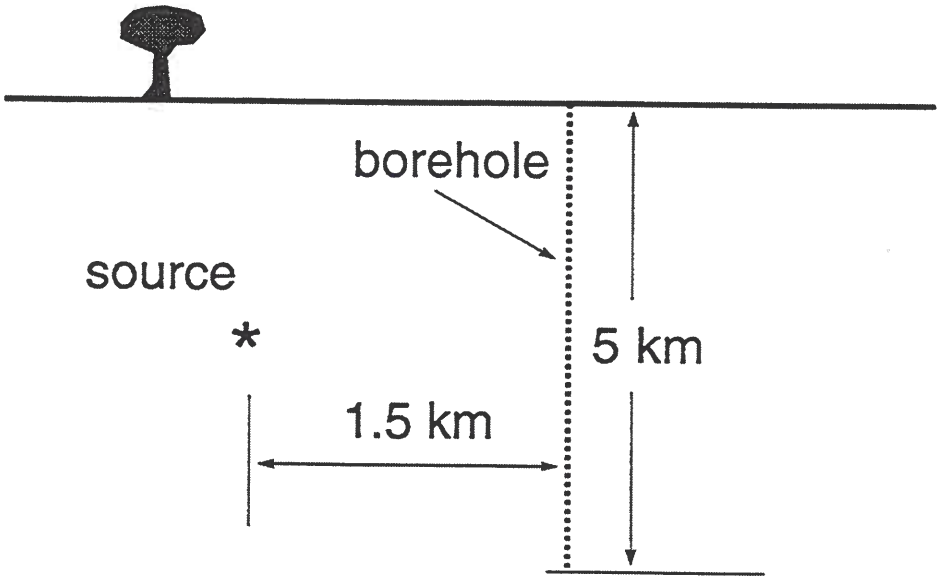

FIG. 7.25. Source and receiver-borehole locations.

$P2$ — reflected P from the surface

$P3$ — reflected P from the left side boundary

$S1$ — direct SV arrival

$S2$ — converted P-SV generated at the surface.

It is easier to identify the various events — direct SH arrival, reflected SH from the surface, and reflected SH from the left side boundary — on the more simple SH-wave data set.

From Figures 7.26 through 7.29, we see that for media that are otherwise the same, but have differing orientations of symmetry axis, the synthetic seismograms vary significantly. When the orientation of the symmetry axis differs from vertical, the recorded seismograms lose their symmetry characteristic. Clearly, then, where the symmetry axis for TI media is tilted, migration algorithms must take that tilt into account in order to order to yield proper positioning of imaged reflectors.

In 2-D problems, the orientation of the symmetry axis is defined by only one parameter θ. However, for 3-D problems, the symmetry axis can be oriented in arbitrary azimuth directions; hence, an extra parameter (the azimuth angle ϕ) must be introduced. This additional variable would significantly increase the complexity of the wave equations and, therefore, of the finite-differencing. However, the FCT correction procedures are the same, and could be applied successfully to 3-D TI media with arbitrary orientation of the symmetry-axis.

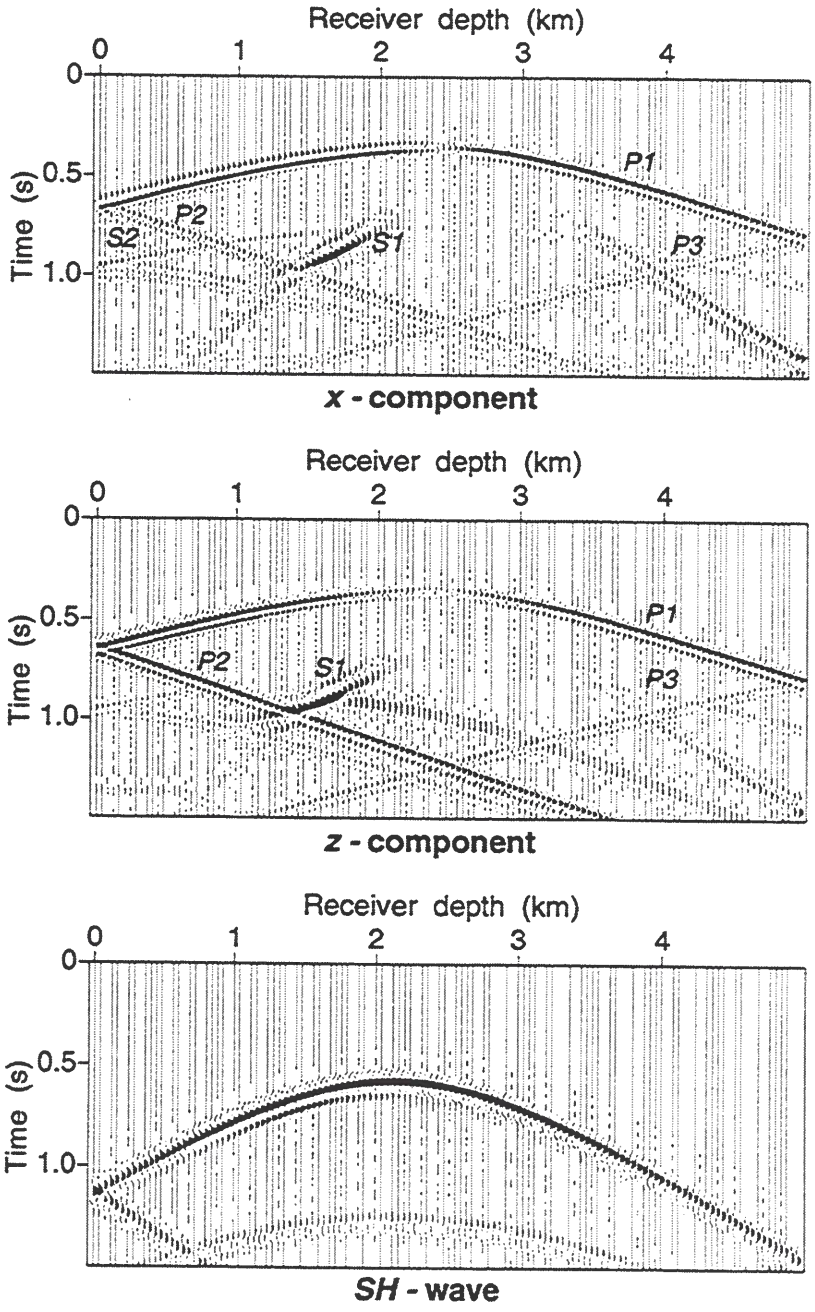

FIG. 7.27. Synthetic seismograms in Mesaverde clayshale with axis of symmetry 30 degrees from vertical. The source is in the vertical direction for the x- and z-component data, and in the y-direction for the SH-wave data.

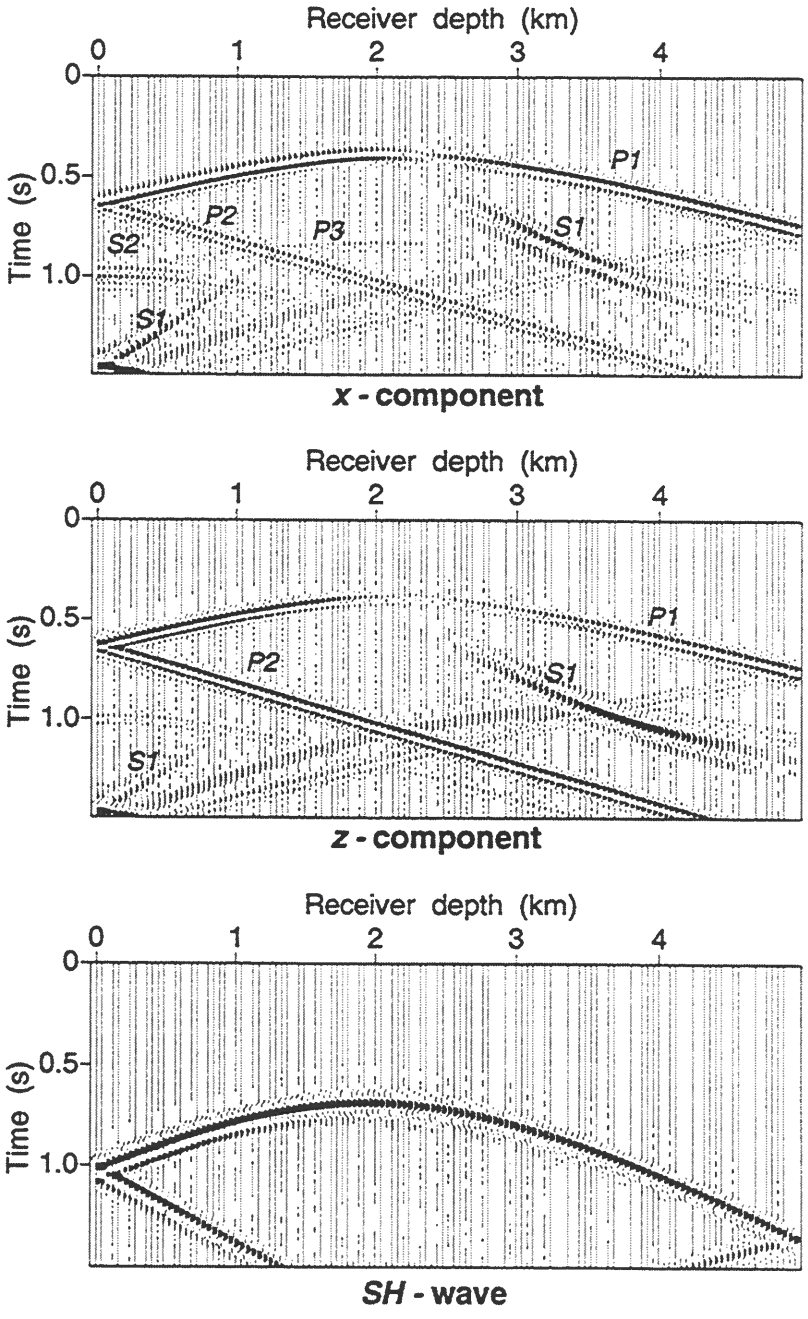

FIG. 7.29. Synthetic seismograms in Mesaverde clayshale with axis of symmetry 60 degrees from vertical. The source is in the vertical direction for the x- and z-component data, and in the y-direction for the SH-wave data.

second-order method. But, then again, applying the FCT correction to the fourth-order method results in both an increase in speed and less memory usage compared to the fourth-order conventional method. So, where does this trade-off between ever-increasing order of finite-differencing versus application of FCT (to higher-order solutions) lead? As suggested by the comparison between the FCT-corrected fourth-order method and the conventional tenth-order finite-difference method in Table 8.1, use of ever-higher order finite-differencing eventually encounters diminishing returns. The speed of the full fourth-order FCT approach is about 28 percent faster, and the memory usage of about 20 percent less than the tenth-order conventional finite-difference method.

Moreover, the optimized FCT method, applied to either the first-order or the second-order differential equation systems, reduces the computational cost of the correction stage of the FCT correction by 40 percent. Hence, the speed of the FCT technique is even greater (Table 8.1).

As seen in Table 8.1, in terms of both computation speed and memory usage, solution of the second-order wave equation is more efficiently accomplished (whether or not the FCT technique is used) than is that of the first-order equations. Instead of solving for one variable in the second-order system [equation (2.1)], three variables for 2-D problems (or four variables for 3-D problems) need to be solved for the first-order system. Therefore, the computational cost and memory usage in the conventional finite-differencing stage (for the first-order equation system) are both increased. Comparing the second-order full FCT and optimized FCT approaches for the two different equation systems, the speed is about 45 percent faster and the memory usage is three times less for the second-order equation system than for the first-order equation system. This argument holds for any order of finite-differencing with the FCT correction.

Although finite-differencing with the FCT correction is more efficient for the second-order equation system than for the first-order equation system, the FCT corrections are easier to code for the first-order system. Moreover, in applications involving elastic media, the conventional finite-differencing itself is easier to code for the first-order system.

For 3-D problems, since the same number of grid points per wavelength (as with the 2-D problems) is required, the efficiency and speed of the FCT method should increase. As seen in Table 8.2, which differs from Table 8.1 only in that it applies to 3-D problems, the speed of the second-order finite-difference method for the second-order equation system increases by a factor of 7.6 when the optimized FCT approach is applied. Application of the optimized FCT correction to the fourth-order method shows particularly strong performance. Moreover, for the second-order equation system, the FCT approach applied to the fourth-order method only requires about 3.8, 30 and 73 percent of the memory used by the second-order, fourth-order and tenth-order finite-difference methods, respectively. Comparing the FCT approach applied to both equation systems, again, as for the 2-D problem, in terms of both speed and memory usage the differencing is best done on the second-order differential equation. Moreover, since the FCT-corrected fourth-order method is more efficient and requires less memory than even the tenth-order conventional finite-difference method, the FCT method therefore is recommended for solving the second-order acoustic wave equation.

Original second-order wave equation (2.1)				
Method	Computational cost proportional to	Points per wavelength (G_0)	Relative speed	Memory
$O(\Delta t^2, \Delta x^2)$	kN^4	11	1	1
$O(\Delta t^2, \Delta x^4)$	$1.6kN^4$	5.5	10	0.125
$O(\Delta t^4, \Delta x^{10})$	$3.6kN^4$	4.1	16	0.052
$O(\Delta t^2, \Delta x^2)$ with FCT	$2.8kN^4$	5.5	5.8	0.125
$O(\Delta t^2, \Delta x^4)$ with FCT	$3.4kN^4$	3.7	22	0.038
$O(\Delta t^2, \Delta x^2)$ with optimized FCT	$2.1kN^4$	5.5	7.6	0.125
$O(\Delta t^2, \Delta x^4)$ with optimized FCT	$2.7kN^4$	3.7	28	0.038
Derived first-order wave equations (2.6) through (2.9)				
Method	Computational cost proportional to	Points per wavelength (G_0)	Relative speed	Memory
$O(\Delta t^2, \Delta x^2)$	$1.6kN^4$	11	0.63	4
$O(\Delta t^2, \Delta x^2)$ with FCT	$4kN^4$	5.5	4.0	0.5
$O(\Delta t^2, \Delta x^2)$ with optimized FCT	$3.1kN^4$	5.5	5.2	0.5

Table 8.2. Same as Table 8.1, but for 3-D acoustic problems.

Full FCT diffusion and anti-diffusion correction			
	acoustic medium	*elastic medium*	cost ratio between *elastic medium* and *acoustic medium*
transport stage	1	3.6	3.6
full FCT corrective stage	1.5	4.5	3
total	2.5	8.1	3.2
ratio of *total* over *transport stage*	2.5	2.3	

Optimized FCT correction			
	acoustic medium	*elastic medium*	cost ratio between *elastic medium* and *acoustic medium*
transport stage	1	3.6	3.6
optimized FCT corrective stage	0.9	2.7	3
total	1.9	6.3	3.3
ratio of *total* over *transport stage*	1.9	1.8	

Table 8.3. Comparison of the relative cost of the FCT method applied to the first-order differential equation system for acoustic and elastic media. The grid size is held constant throughout. Here, the computation effort for solving the first-order acoustic wave equations is taken as unity, for reference.

Full FCT diffusion and anti-diffusion correction			
	acoustic medium	*elastic medium*	cost ratio between *elastic medium* and *acoustic medium*
transport stage	1	3.6	3.6
full FCT corrective stage	1.8	5.4	3
total	2.8	9.0	3.2
ratio of *total* over *transport stage*	2.8	2.5	

Optimized FCT correction			
	acoustic medium	*elastic medium*	cost ratio between *elastic medium* and *acoustic medium*
transport stage	1	3.6	3.6
optimized FCT corrective stage	1.1	3.3	3
total	2.1	6.9	3.3
ratio of *total* over *transport stage*	2.1	1.9	

Table 8.4. Comparison of the relative cost of the FCT method applied to the second-order differential equation system for acoustic and elastic media. Here, the computation effort for solving the second-order acoustic wave equation is taken as unity, for reference.

in the elastic-wave equations is greater than that for the acoustic-wave equation. In contrast, the FCT computational effort for each variable is the same as that for the acoustic wave equation. Therefore the efficiency gains for the FCT method are larger for elastic media than for acoustic media.

When using higher-order methods in the finite-differencing step, the relative computational cost of the FCT method is reduced since the FCT correction is independent of the order of finite-differencing. Moreover, because the use of finite-differencing of ever increasing order encounters diminishing returns, application of the FCT correction to the fourth-order finite-difference method, for example, offers greater computation and memory savings than does the conventional tenth-order method.

Despite the benefits of the FCT corrections, the computation effort of reverse-time depth migration is still about three to ten times (depending on the velocity model) that of the Kirchhoff integral method for 2-D migration. For 3-D migration and modeling, the computational effort of any finite-difference method (the FCT method in particular) is proportional to N^4, while that of the Kirchhoff integral method or Gaussian beam method is proportional to N^5, suggesting that, for 3-D problems, the finite-difference method with the FCT correction might become cost-competitive with the Kirchhoff integral method or Gaussian beam method.

The computer codes related to this work are located at the Center for Wave Phenomena, Colorado School of Mines. For application in acoustic media, four codes are available, while for applications in elastic media, one code is available. These codes and their application areas are listed below.

1. **fctmod.c** — finite-difference modeling for 2-D acoustic media with the full FCT correction.

2. **fctmig.c** — finite-difference migration for 2-D acoustic media with the full FCT correction.

3. **fctmodopt.c** — finite-difference modeling for 2-D acoustic media with the optimized FCT correction.

4. **fctmigopt.c** — finite-difference migration for 2-D acoustic media with the optimized FCT correction.

5. **fctanis.c** — finite-difference modeling for 2-D elastic and transversely isotropic media with the full FCT correction. The code can also be used for migration.

In this work, I have only briefly studied the dependence of the solutions on the diffusion and anti-diffusion coefficients η_1, η_2 and η. I suggest further detailed study of these parameters, either theoretical or empirical. A developed relationship between the optimum values of these coefficients and the coarseness of the grid (i.e., number of grid points per upper half-power wavelength) and the order of finite-differencing would be helpful. Also, in this work, the FCT technique has been applied to only one field data set. The advantages of the FCT method would best be demonstrated through testing with

REFERENCES

Alford, R., Kelly, K., and Boore, D., 1974, Accuracy of finite-difference modeling of the acoustic wave equation: Geophysics, **39**, 834-842.

Aminzadeh, F., Burkhard, N., Nicoletis, L., Rocca, F., Wyatt, K., 1994, SEG/EAEG 3-D modeling project: 2nd update: The Leading Edge, **13**, 949-952.

Backus, G. E., 1962, Long-wave elastic anisotropy produced by horizontal layering: J. Geophys. Res., **67**, 4427-4440.

Blacquiere, G., Debeye, H., Wapenaar, C., and Berkhout, A., 1989, 3D table-driven migration: Geophys. Prosp., **37**, 925-958.

Bleistein, N., 1974, Asymptotic analysis of finite-difference schemes: Unpublished manuscript.

Bleistein, N., 1984, Mathematical methods for wave phenomena: Academic Press, Inc.

Bleistein, N., and Handelsman, R. A., 1986, Asymptotic expansions of integrals: Dover Publications, Inc., New York

Bleistein, N., 1994, Colorado School of Mines: Private communication.

Boris, J. P., and Book, D. L., 1973, Flux-corrected transport. I. SHASTA, A fluid transport algorithm that works: J. Comput. Phys., **11**, 38-69.

Book, D. L., Boris, J. P., and Hain, K., 1975, Flux-corrected transport II: generalization of the method: J. Comput. Phys., **18**, 248-283.

Carrier, G. F, Krook, M., and Pearson, C. E., 1983, Function of a complex variable: Hod Books, Ithaca, New York, p438.

Claerbout, J., 1985, Imaging of the earth's interior: Blackwell Scientific Publications, Inc.

Clayton, R., and Engquist, B., 1980, Absorbing side boundary conditions for wave equation migration: Geophysics, **45**, 895-904.

Dablain, M. A. 1986, The application of high-order differencing to the scalar wave equation: Geophysics, **51**, 54-66.

Ewing, R. E., Sharpley, R. C., Mitchum, D., O'Leary, P., and Sochacki, J. S., 1994, Distributed computation of wave propagation models using PVM: IEEE Parallel & Distributed Technology, 2, 26-31.

Appendix A

ASYMPTOTIC ANALYSIS OF THE LEAPFROG SCHEME

In this appendix, I use z-transforms and asymptotic analysis for large time to analyze damping in the leapfrog scheme. This method, which provides an analytical check on the finite-difference schemes, was proposed by Bleistein (1974). Also, in this appendix, I give a direct comparison of the asymptotic solution and the leapfrog solution.

Let's consider a solution continuous in time, discrete in space, where the essence of the leapfrog scheme resides. Thus, I rewrite equations (3.3) and (3.4) as

$$\frac{\partial u_{j+1/2}}{\partial t} = \epsilon_1 (q_{j+1} - q_j), \tag{A.1}$$

$$\frac{\partial q_j}{\partial t} = \epsilon_2 \left(u_{j+\frac{1}{2}} - u_{j-\frac{1}{2}} \right), \tag{A.2}$$

where $\epsilon_1 \equiv \rho c^2/\Delta x$, $\epsilon_2 \equiv 1/\rho \Delta x$, and Δx is the spatial step. In the examples shown later, I use a constant velocity of 2 km/s.

The finite-difference equations will be solved by the z-transform (Oppenheim, et al., 1983). To do so (Bleistein, 1994), I introduce

$$U(z) = \sum_{-\infty}^{\infty} u_{\frac{k}{2}} z^k, \tag{A.3}$$

$$Q(z) = \sum_{-\infty}^{\infty} q_{\frac{k}{2}} z^k. \tag{A.4}$$

Multiplying both side of equations (A.1) and (A.2) by z^{2j+2} and z^{2j}, respectively, I obtain

$$\frac{\partial}{\partial t} \left(u_{j+\frac{1}{2}} z^{2j+2} \right) = \epsilon_1 \left(q_{j+1} z^{2j+2} - q_j z^{2j+2} \right), \tag{A.5}$$

$$\frac{\partial}{\partial t} \left(q_j z^{2j} \right) = \epsilon_2 \left(u_{j+\frac{1}{2}} z^{2j} - u_{j-\frac{1}{2}} z^{2j} \right). \tag{A.6}$$

Taking the summation of these equations over the index j, produces

$$\frac{\partial}{\partial t} \left(z \sum_j u_{j+\frac{1}{2}} z^{2j+1} \right) = \epsilon_1 \left(\sum_j q_{j+1} z^{2j+2} - z^2 \sum_j q_j z^{2j} \right), \tag{A.7}$$

$$\frac{\partial}{\partial t} \left(\sum_j q_j z^{2j} \right) = \epsilon_2 \left(\frac{1}{z} \sum_j u_{j+\frac{1}{2}} z^{2j+1} - z \sum_j u_{j-\frac{1}{2}} z^{2j-1} \right). \tag{A.8}$$

formulas (Carrier et al., 1983):

$$u_{j+\frac{1}{2}} = \frac{1}{2\pi i}\oint_{C'} \frac{U_o}{z^{2j+2}} dz, \tag{A.18}$$

where C' is a unit circle.

Using solution (A.17), we then have,

$$\begin{aligned} u_{j+\frac{1}{2}} &= \sum_{\pm} \frac{1}{4\pi i}\oint_{C'} \frac{1}{z^{2j+2}} \frac{(1+z^2)}{z} \exp\left[\pm\epsilon t\left(z-\frac{1}{z}\right)\right] dz \\ &= \sum_{\pm} \frac{1}{4\pi i}\oint_{C'} \frac{1}{z^{2j+1}} \left(\frac{1}{z^2}+1\right) \exp\left[\pm\epsilon t\left(z-\frac{1}{z}\right)\right] dz. \end{aligned} \tag{A.19}$$

Thus, integration by parts yields

$$u_{j+\frac{1}{2}} = -\frac{1}{4\pi i}\frac{(2j+1)\Delta x}{ct} \sum_{\pm} \pm \oint_{C'} \frac{dz}{z^{2j+2}} \exp\left[\pm\epsilon t\left(z-\frac{1}{z}\right)\right]. \tag{A.20}$$

Since $1/z^{2j+1} = \exp[-(2j+1)\log z]$, the above integral can then be rewritten as

$$u_{j+\frac{1}{2}} = \frac{1}{4\pi i}\frac{(2j+1)\Delta x}{ct} \sum_{\pm} \mp \oint_{C'} \frac{dz}{z} \left[e^{\phi_{\pm}(z)}\right], \tag{A.21}$$

where

$$\phi_{\pm}(z) = -2(j+\frac{1}{2})\log z \pm \epsilon t\left(\frac{1}{z}-z\right). \tag{A.22}$$

Since $\epsilon = c/\Delta x$, equation (A.22) can be rewritten as

$$\phi_{\pm}(z) = \left[-2\left(\frac{x}{ct}\right)\log z \pm \left(\frac{1}{z}-z\right)\right]\frac{ct}{\Delta x}, \tag{A.23}$$

where $x = (j+\frac{1}{2})\Delta x$.

Equation (A.23) can be further rewritten as

$$\phi_{\pm}(z) = \lambda w_{\pm}(z,\theta), \tag{A.24}$$

where $\lambda = ct/\Delta x$, $\theta = x/ct$ and

$$w_{\pm}(z,\theta) = -2\theta\log z \pm \left(\frac{1}{z}-z\right). \tag{A.25}$$

The integral (A.21) can then be expressed as

$$u_{j+\frac{1}{2}} = \frac{\theta}{2\pi i} \sum_{\pm} \mp \oint_{C'} \frac{dz}{z} \exp\left[\lambda w_{\pm}(z,\theta)\right], \tag{A.26}$$

This is the form to which we can apply asymptotic analysis by the method of steepest

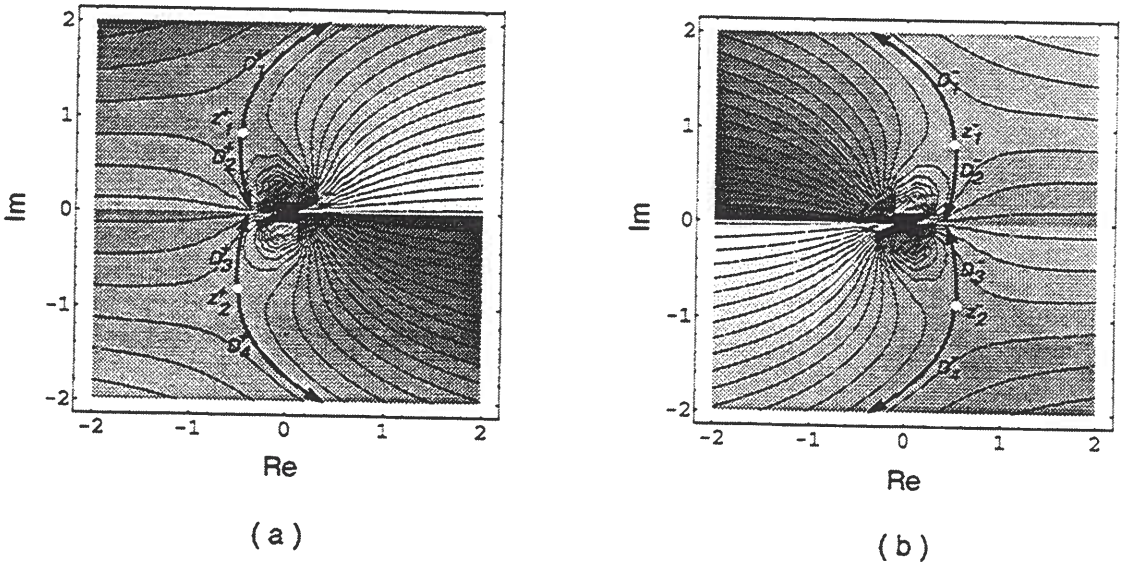

FIG. A.1. Contour plots showing the saddle points and the steepest descent paths for $\theta = 0.5$. (a) is for $w_+(z,\theta)$, and (b) is for $w_-(z,\theta)$.

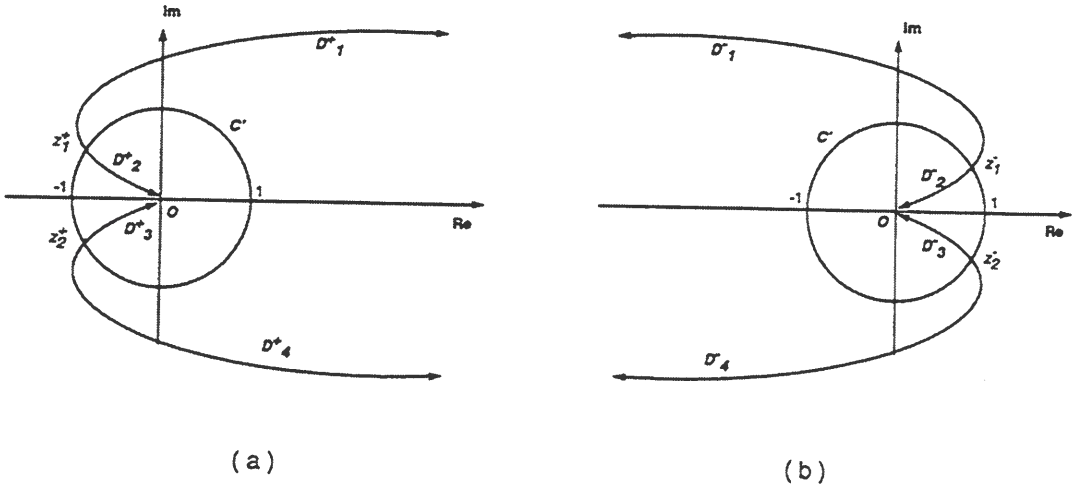

FIG. A.2. Schematic plots showing the saddle points and the steepest descent paths for $\theta = 0.5$. (a) is for $w_+(z,\theta)$, and (b) is for $w_-(z,\theta)$.

of them are located outside the unit circle while the other two are located inside the unit circle. Figures A.4a and A.4b give the contour plots of the imaginary parts of $w_+(z,\theta)$ and $w_-(z,\theta)$, respectively, for the case $\theta = 2$. Moreover, both figures show the saddle points and the steepest descent paths. Similar to the discussion for $\theta < 1$, the contour integral (A.26) can also be replaced by integrating over the steepest descent contours. However, in this case, only the saddle points z_1^+ and z_1^- contribute to the integration.

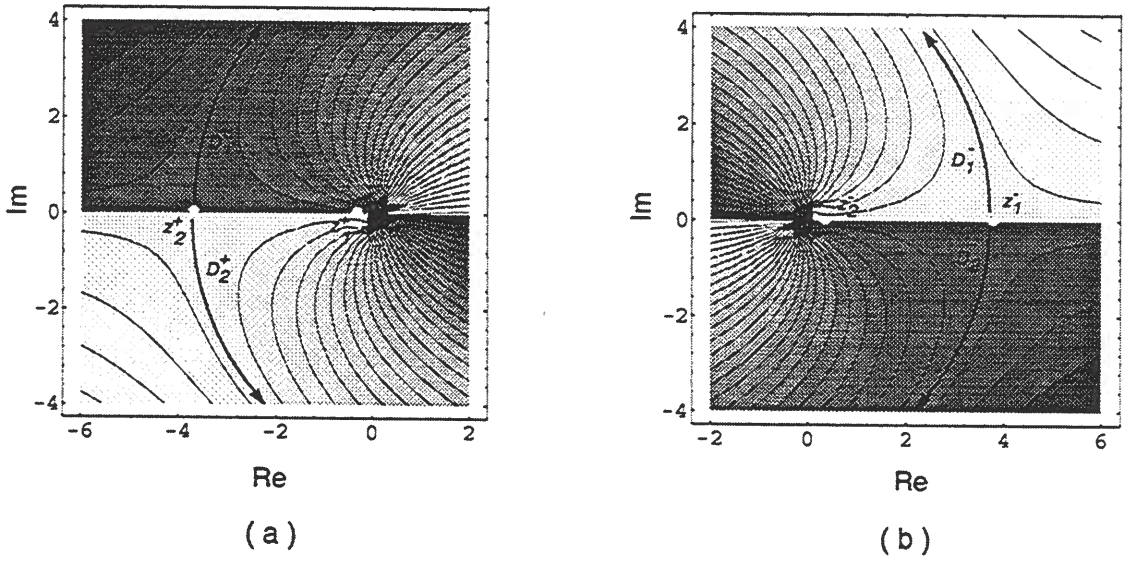

FIG. A.4. Contour plots showing the saddle points and the steepest descent paths for $\theta = 2$. (a) is for $w_+(z)$, and (b) is for $w_-(z)$.

After replacing the contour C' by the steepest descent contours, the new integral becomes

$$u_{j+\frac{1}{2}} = \frac{\theta}{2\pi i}\left\{\left[-\int_{D_1^+} + \int_{D_2^+}\right] e^{\lambda w_+(z,\theta)}\frac{dz}{z} + \left[\int_{D_1^-} - \int_{D_2^-}\right] e^{\lambda w_-(z,\theta)}\frac{dz}{z}\right\}. \qquad \text{(A.37)}$$

Therefore, as for the case $\theta = 0.5$, the asymptotic expansion of this integral (A.37) can be explicitly expressed as a function of λ and θ,

$$u_{j+\frac{1}{2}} \sim \frac{\theta}{\pi}\sqrt{\frac{\pi}{\lambda\sqrt{\theta^2-1}}}\exp\left[-2\lambda\left(\theta\log|\theta+\sqrt{\theta^2-1}| - \sqrt{\theta^2-1}\right)\right]. \qquad \text{(A.38)}$$

From expression (A.38), we see that the amplitude decays exponentially as λ increases.

Figure A.5 gives the solution $u_{j+1/2}$ as a function of λ (for $\theta = 2$). The result shows that as λ increases, the wavefield amplitude has an exponential decay forward of the wavefront.

Now, let us consider the situation at the wavefront, i.e., for the case of $\theta = 1.0$. Again, as for the previous two cases, Figure A.6 shows the saddle points and the steepest

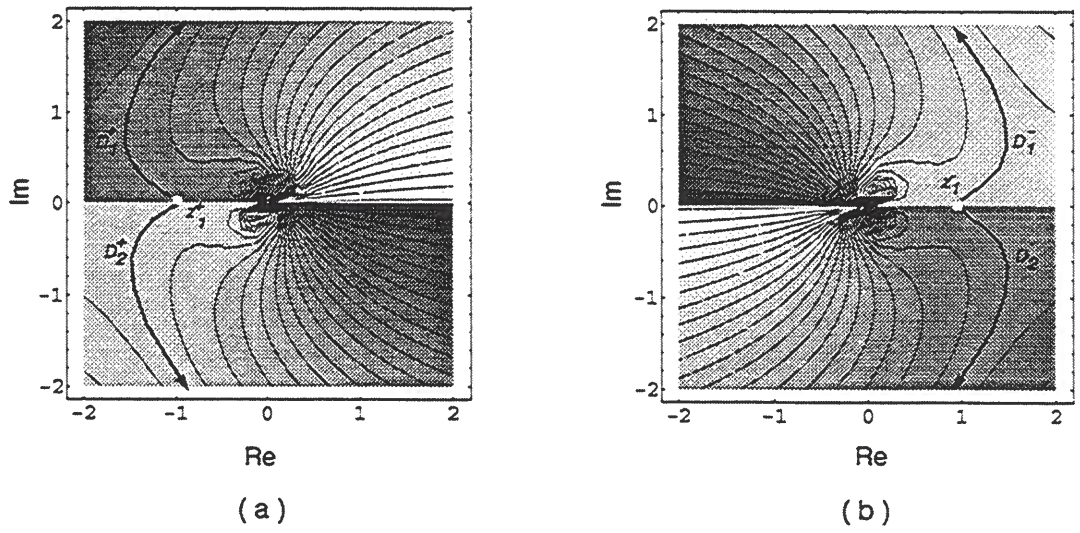

FIG. A.6. Contour plots showing the saddle points and the steepest descent paths for $\theta = 1$. (a) is for $w_+(z,\theta)$, and (b) is for $w_-(z,\theta)$.

been converted to the same distance scale as used in the leapfrog solution. The figure shows that both the asymptotic approach and the leapfrog method produce about the same peak amplitude and both decay with distance. Also, from Figure A.8, we see that the asymptotic solution can better predict the peak amplitude for the first event than for the two later events, since the later events are interfering with the oscillation tails from the events ahead.

A direct comparison of the wavefield snapshot obtained by the asymptotic approach and the leapfrog method is shown in Figures A.9 and A.10. For both methods, the same impulsive source is used. Comparing Figures A.9 and A.10, we see that the asymptotic solution is similar to the solution obtained by the leapfrog method.

The above examples and discussion demonstrate that for a broad band solution containing frequencies up to Nyquist frequency, the asymptotic approach and the leapfrog finite-difference method produce similar results. Now, a logical question is whether or not the finite-difference method and the asymptotic approach produce similar results for low-frequency (relative to the Nyquist frequency) wave propagation.

To examine the asymptotic approach and the finite-difference method for low-frequency wave propagation, I adapt the previous results for high-frequency wave propagation. Filtering the impulsive initial condition with a 5-Hz, low-pass filter, gives the low-frequency initial condition shown in Figure A.11 (the maximum frequency of the low-pass filter is ten percent of the Nyquist frequency, $1/2\Delta t_{max}$, in the leapfrog scheme; here, Δt_{max} is the maximum time step allowed in the finite-difference scheme). The asymptotic solution for this low-frequency initial condition can be obtained by filtering the solution for the impulsive source (Figure A.9). Here, the filter should be the same as that used in filtering the initial condition. Figure A.12 gives the wavefield snapshot at 1 s ($\lambda = 100 >> 1$) obtained by the asymptotic approach. The solution shows no dispersive error. More-

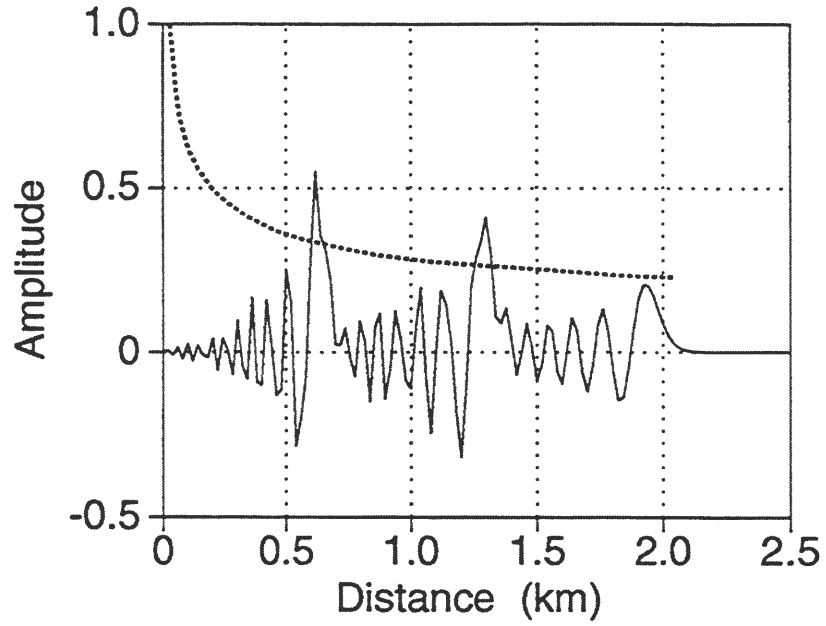

FIG. A.8. Wavefield snapshot produced by the leapfrog scheme ($\Delta x = 0.02$ km) for three isolated impulses. The dashed line indicates the wavefield amplitude obtained by the asymptotic approach.

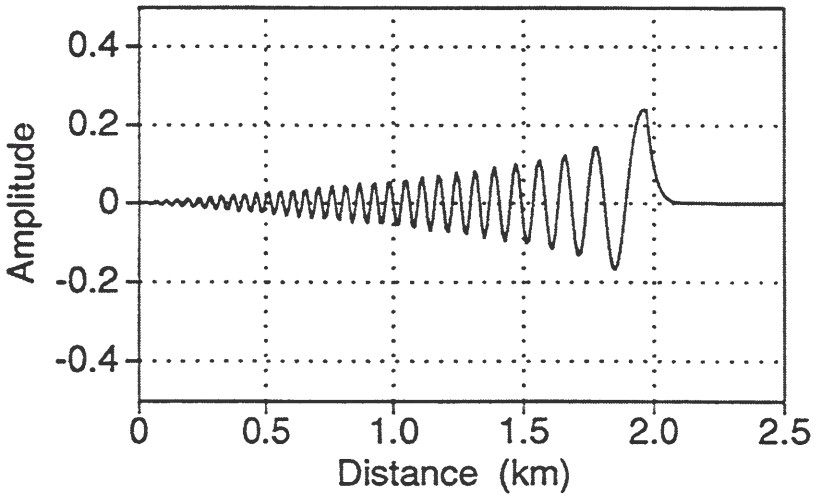

FIG. A.9. Wavefield snapshot generated by the asymptotic approach for an impulsive source.

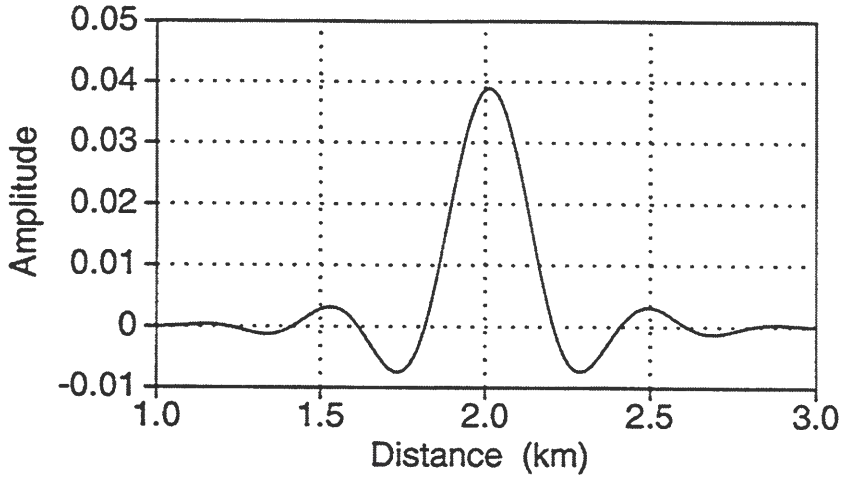

FIG. A.12. Wavefield snapshot ($t = 1s$) generated by the asymptotic approach for the low-frequency initial condition given in Figure A.11.

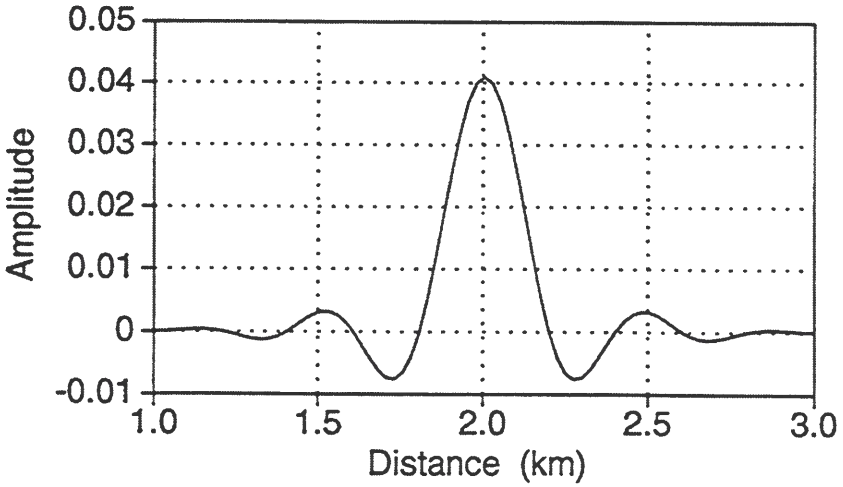

FIG. A.13. Wavefield snapshot ($t = 1s$) produced by the leapfrog scheme for the low-frequency initial condition given in Figure A.11. The spatial step is $\Delta x = 0.02$ km.

where $0 \leq \eta_2 \leq 1$. The values of η_2 may differ from those of η_1. Since the amplitude and resolution losses are introduced in two ways; from the conventional finite-differencing and from artificial added diffusion, we would like the anti-diffusion to compensate not only the artificial diffusion but also the amplitude loss in the conventional finite-differencing. Therefore, we generally use η_2 about 10 to 15 percent larger than η_1.

4. Modify (i.e. *diffuse*) the solution q using Q_x, Q_y and Q_z; this process smooths the solution (also causes an undesirable loss of amplitude) and eliminates the ripples caused by grid dispersion:

$$\begin{aligned} \tilde{q}^{n+1}_{i,j,k} = q^{n+1}_{i,j,k} \quad &+ \quad (Q_{x}{}^{n-1}_{i+1/2,j,k} - Q_{x}{}^{n-1}_{i-1/2,j,k}) \\ &+ \quad (Q_{y}{}^{n-1}_{i,j+1/2,k} - Q_{y}{}^{n-1}_{i,j-1/2,k}) \\ &+ \quad (Q_{z}{}^{n-1}_{i,j,k+1/2} - Q_{z}{}^{n-1}_{i,j,k-1/2}). \end{aligned} \tag{B.3}$$

5. Take the differences of the diffused $\tilde{q}$:

$$\begin{aligned} X_{i+1/2,j,k} &= \tilde{q}^{n+1}_{i+1,j,k} - \tilde{q}^{n+1}_{i,j,k} \\ Y_{i,j+1/2,k} &= \tilde{q}^{n+1}_{i,j+1,k} - \tilde{q}^{n+1}_{i,j,k} \\ Z_{i,j,k+1/2} &= \tilde{q}^{n+1}_{i,j,k+1} - \tilde{q}^{n+1}_{i,j,k}. \end{aligned} \tag{B.4}$$

6. *Anti-diffuse* the solution as follows, and obtain the corrected solution for q :

$$\begin{aligned} q^{n+1}_{i,j,k} = \tilde{q}^{n+1}_{i,j,k} \quad &- \quad (X^c_{i+1/2,j,k} - X^c_{i-1/2,j,k}) - (Y^c_{i,j+1/2,k} - Y^c_{i,j-1/2,k}) \\ &- \quad (Z^c_{i,j,k+1/2} - Z^c_{i,j,k-1/2}), \end{aligned} \tag{B.5}$$

where

$$\begin{aligned} X^c_{i+1/2,j,k} &= S_x \max\{0, \min[S_x X_{i-1/2,j,k}, \mathrm{abs}(\tilde{Q}_{x}{}^{n+1}_{i+1/2,j,k}), S_x X_{i+3/2,j,k}]\}, \\ Y^c_{i,j+1/2,k} &= S_y \max\{0, \min[S_y Y_{i,j-1/2,k}, \mathrm{abs}(\tilde{Q}_{y}{}^{n+1}_{i,j+1/2,k}), S_y Y_{i,j+3/2,k}]\}, \\ Z^c_{i,j,k+1/2} &= S_z \max\{0, \min[S_z Z_{i,j,k-1/2}, \mathrm{abs}(\tilde{Q}_{z}{}^{n+1}_{i,j,k+1/2}), S_z Z_{i,j,k+3/2}]\}, \\ S_x &= \mathrm{sign}\{\tilde{Q}_{x}{}^{n+1}_{i+1/2,j,k}\}, \\ S_y &= \mathrm{sign}\{\tilde{Q}_{y}{}^{n+1}_{i,j+1/2,k}\}, \\ S_z &= \mathrm{sign}\{\tilde{Q}_{z}{}^{n+1}_{i,j,k+1/2}\}. \end{aligned}$$

For elastic media, the same general FCT correction procedures can be applied to the first-order system of elastic wave equations. Similar to the acoustic case, such correction procedures need only be applied to the variables v_1, v_2 and v_3. Once v_1, v_2 and v_3 are corrected, e_{pq} can be computed directly from equation (2.14).

5. Compute diffusive fluxes with the diffused $\tilde{P}^{n+1}$ and P^n:

$$\begin{aligned} X_{i+1/2,j,k} &= (\tilde{P}^{n+1}_{i+1,j,k} - \tilde{P}^{n}_{i+1,j,k}) - (\tilde{P}^{n+1}_{i,j,k} - \tilde{P}^{n}_{i,j,k}) \\ Y_{i,j+1/2,k} &= (\tilde{P}^{n+1}_{i,j+1,k} - \tilde{P}^{n}_{i,j+1,k}) - (\tilde{P}^{n+1}_{i,j,k} - \tilde{P}^{n}_{i,j,k}) \\ Z_{i,j,k+1/2} &= (\tilde{P}^{n+1}_{i,j,k+1} - \tilde{P}^{n}_{i,j,k+1}) - (\tilde{P}^{n+1}_{i,j,k} - \tilde{P}^{n}_{i,j,k}). \end{aligned} \tag{C.4}$$

6. *Anti-diffuse* the solution as follows, and obtain the corrected solution for P :

$$\begin{aligned} P^{n+1}_{i,j,k} = \tilde{P}^{n+1}_{i,j,k} \quad &- \quad (X^c_{i+1/2,j,k} - X^c_{i-1/2,j,k}) - (Y^c_{i,j+1/2,k} - Y^c_{i,j-1/2,k}) \\ &- \quad (Z^c_{i,j,k+1/2} - Z^c_{i,j,k-1/2}), \end{aligned} \tag{C.5}$$

where $X^c_{i+1/2,j,k}$, $Y^c_{i,j+1/2,k}$ and $Z^c_{i,j,k+1/2}$ are given in step 6 of Appendix B.

Similar to the first-order system, the above FCT correction procedures can be applied to elastic wave equation (2.10).

caused by grid dispersion:

$$\begin{aligned} q_{i,j,k}^{n+1} = q_{i,j,k}^{n+1} \quad &+ \quad (Q_x^{c\ n}_{\ i+1/2,j,k} - Q_x^{c\ n}_{\ i-1/2,j,k}) \\ &+ \quad (Q_y^{c\ n}_{\ i,j+1/2,k} - Q_y^{c\ n}_{\ i,j-1/2,k}) \\ &+ \quad (Q_z^{c\ n}_{\ i,j,k+1/2} - Q_z^{c\ n}_{\ i,j,k-1/2}). \end{aligned} \tag{D.3}$$

Similar to the FCT diffusion and anti-diffusion corrections given in Appendix B for the first-order system equations, the optimized FCT procedures can be applied to the first-order elastic wave equations as well.

caused by grid dispersion:

$$\begin{aligned} P_{i,j,k}^{n+1} = P_{i,j,k}^{n+1} &+ (Q_x^{c\ n}_{i+1/2,j,k} - Q_x^{c\ n}_{i-1/2,j,k}) \\ &+ (Q_y^{c\ n}_{i,j+1/2,k} - Q_y^{c\ n}_{i,j-1/2,k}) \\ &+ (Q_z^{c\ n}_{i,j,k+1/2} - Q_z^{c\ n}_{i,j,k-1/2}). \end{aligned} \tag{E.3}$$

Similar to the full FCT correction steps listed in Appendix C, the optimized FCT procedures for the second-order system can be applied to the elastic wave equation (2.10) as well.